ACS APPLIED OPTICAL MATERIALS

pubs.acs.org/acsaom

Article

Tert-Butylcarbazole and Methoxycarbazole Substituted on the Phenazine Group Exhibit Mechano and Thermoresponsivity for TADF LEECs

Marzieh Rabiei,* Mozhgan Hosseinnezhad, Raheleh Ghahary, Venkatramaiah Nutalapati, Sohrab Nasiri,* Jean-Michel Nunzi, Juozas Padgurskas, and Raimundas Rukuiza

Cite This: https://doi.org/10.1021/acsaom.5c00065

Read Online

ACCESS | Metrics & More | Article Recommendations | Supporting Information

ABSTRACT: Two new well-defined donor−acceptor−donor (D−A−D′) thermally activated delayed fluorescence (TADF) molecules with mechanochromic and thermochromic architectures were designed and synthesized based on *tert*-butylcarbazole and methoxycarbazole substituents attached to a phenazine derivative. Density functional theory (DFT) studies revealed molecular structures with extended π-conjugation and low singlet−triplet energy gaps (ΔE_{ST}), which enhance reverse intersystem crossing (RISC) for efficient TADF. Single-crystal X-ray diffraction confirms differences in molecular packing. The dye composed of *tert*-butylcarbazole exhibits lower aggregation and higher photoluminescence quantum yield (PLQY) upon spin-coating in a solid film, owing to its bulkier structure. Thermal stability studies demonstrated high decomposition temperatures ($T_d > 300$ °C) and improved rigidity of the dye consisting of *tert*-butylcarbazole. Photophysical investigations revealed that the dyes dispersed in a tetrahydrofuran (THF):water mixture showed aggregation-induced emission enhancement (AIEE). Incorporation of the complex organometallic [Ir(buoppy)$_2$(dmapzpy)]PF$_6$ as a host in LEECs favors the energy transfer and yields single emission peaks at 588 and 587 nm with 60 wt % host content. The improved device attains maximum current (28.97 cd A^{-1}), power (22.11 lm W^{-1}), and external quantum efficiency (4.02%). These findings underline the significance of substituent design and host:guest interactions in improving TADF LEEC performance and provide new insights for high-efficiency optoelectronic devices.

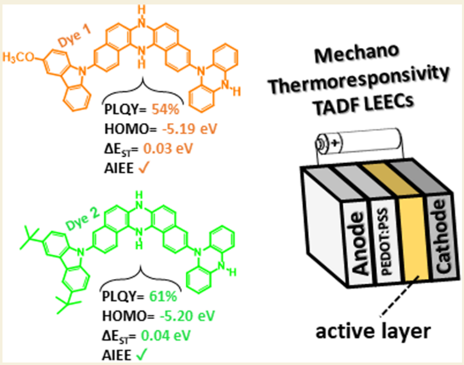

KEYWORDS: *phenazine, tert-butylcarbazole, methoxycarbazole, mechanochromism, thermochromism, TADF, LEECs*

1. INTRODUCTION

The advancement of optical devices depends on innovative materials and designs to meet the growing demands for efficiency and functionality. The development of light-emitting electrochemical cells (LEECs) has attracted considerable attention due to their potential for low-cost and efficient devices.[1] Most challenges in LEECs require advances in material design, such as thermally activated delayed fluorescence (TADF) emitters, stable hosts, better device architectures, and improved fabrication techniques to increase the efficiency, stability, and overall performance of the LEECs.[2−4] The development of molecules for TADF is complex due to several interdependent factors that must be optimized for efficient performance.[5] Key challenges in the development of TADF molecules include energy level balancing, molecular architecture optimization, photophysics and stability tradeoff, color tuning, device integration, and synthetic complexity.[6] TADF materials exhibit both prompt and delayed fluorescence, with the delayed fluorescence resulting from thermal activation of triplet excitons.[7] Dual emission makes them efficient in utilizing excitons for light generation and enables an internal quantum efficiency (IQE) reaching nearly 100%.[8] However, at high excitation densities, phenomena such as triplet−triplet annihilation (TTA) and exciton quenching can reduce the efficiency. Unlike phosphorescent materials, which rely on heavy metal complexes to generate triplet excitons, TADF materials are metal-free, making them less expensive and more environmentally friendly. In addition, TADF performance is temperature-dependent due to the thermal dependence of reverse intersystem crossing (RISC), with efficiency decreasing at lower temperatures.[9] Several stimuli-dependent mechanisms such as mechanochromism and thermochromism lead to a change in the optical properties of a material.[10] These mechanisms are particularly interesting for the development

Received: February 15, 2025
Revised: June 17, 2025
Accepted: June 18, 2025

Scheme 1. Synthesis Pathway of the Organic Dyes

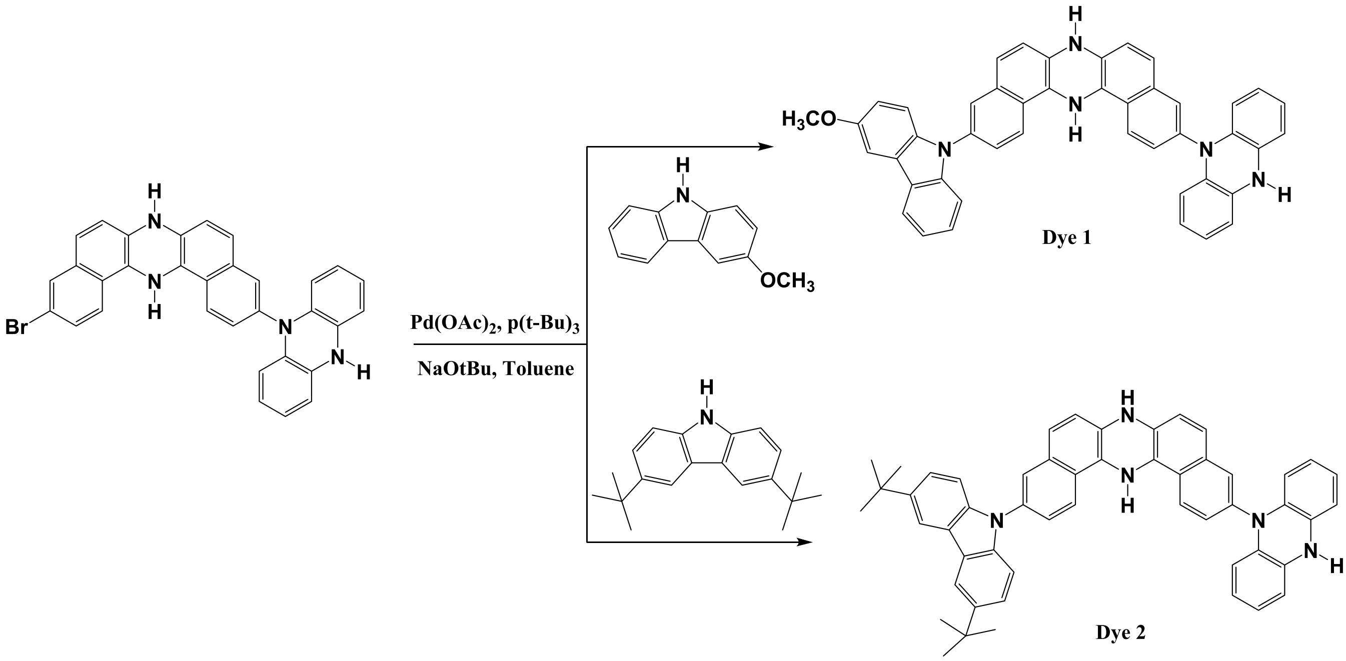

of modern materials for sensors, smart devices, and optoelectronics. Mechanochromism refers to the property of materials that exhibit a color change in response to mechanical stimuli such as grinding, pressing, stretching, shearing, or scratching.[11] These materials change their photophysical or optical properties due to changes in their molecular structure, packing, or interactions caused by mechanical forces.[12] Thermoresponsiveness is the property of materials that exhibit a color change in response to temperature variations. This phenomenon occurs due to changes in the molecular structure, electronic state, or aggregation behavior of the material upon heating or cooling.[13] Donor−acceptor−donor (D−A−D′) molecular architectures are commonly used in the design of organic semiconductors, light-emitting materials, and other optoelectronic compounds. Electron-donating groups donate electrons to the central acceptor unit. Electron-withdrawing groups stabilize the electrons transferred by the donors. The use of different donor units (D, D′) leads to an asymmetry that allows fine-tuning of the energy levels, dipole moment, and optical properties of the molecules.[14] D and D′ can have different steric or electronic properties that influence charge transfer and molecular packing.[15] Phenazine is a nitrogen-containing aromatic heterocycle with chemical formula $C_{12}H_8N_2$; it is a tricyclic compound composed of two benzenes and one pyrazine ring.[16] The nitrogen atoms in the pyrazine ring contribute to its unique electronic properties. Phenazine derivatives are widely used in organic semiconductors, organic light-emitting diodes (OLEDs), and solar cells due to their favorable charge transport and light emission properties.[17] The incorporation of donor−acceptor groups into the phenazine core enables precise tuning of the photophysical and electronic properties.[18] Modified phenazine structures can serve as efficient acceptor units in TADF emitters for efficient light-emitting devices. In this study, substituted carbazole derivatives were prepared to design light-emitting molecules with thermoresponsive properties. The designed molecules are metal-free, which is of interest from an environmental perspective, and easier to synthesize than organomineral compounds. They provide convenient mechanical properties. Analytical and computational techniques were used to investigate the performance of the prepared molecules. Their photochemical and electrochemical responses were studied. The synthesis route of the dyes is shown in Scheme 1.

2. EXPERIMENTAL SECTION

Intermediates, dyes, and other chemical compounds, including solvents, organic reactants, and catalysts, used in the synthesis process were purchased from Merck & Aldrich Co. and used without purification. The synthesis of compound A is described in the Supporting Information.

2.1. Synthesis of Dyes 1 and 2

A mixture of A (1 mmol), secondary amine (1.2 mmol), $Pd (OAC)_2$ (0.020 mmol), tri-*tert*-butylphosphine (0.04 mmol), and sodium *tert*-butoxide (1.5 mmol) was prepared in 5 mL of toluene and stirred under a nitrogen atmosphere for 6 h at 120 °C. The mixture was gradually cooled and poured into a mixture of water (3 mL) and ethyl acetate (20 mL). The organic and aqueous layers were separated and dried completely using magnesium sulfate and rotary evaporation.

2.1.1. 3-Phenazine,11-(5-methocycarbazole)dibenzo[*a*,*j*]-phenazine (Dye 1). ^{1}H NMR (500 MHz, chloroform, δ/ppm): 8.33 (1H, s), 8.11−8.07 (4H, d, J = 7.5 Hz), 8.02−7.91 (4H, m), 7.85−7.77 (4H, m), 7.76 (3H, s), 7.63 (3H, d, J = 7.3 Hz), 7.48−7.45 (2H, d, J= *7.3 Hz*), 7.26 (2H, t), 6.63−6.55 (3H, d, J = 7.2 Hz), 5.80 (2H, s), 8.87 (3H, s, OCH_3); ^{13}CNMR (500 MHz, chloroform, δ/ppm): 155, 147, 143, 142, 141, 140, 138, 138, 135, 131, 131, 129, 128, 128, 127, 126, 125, 125 (3C), 124 (2C), 123, 122 (2C), 121, 120 (2C), 119, 115, 113, 112, 110, 105 (Ar.), 67 (aliphatic). Beige-white with a bluish tint solid, 83% yield.

2.1.2. 3-Phenazine,11-(3,6-di-*tert*-butylcarbazole)dibenzo-[*a*,*j*]phenazine (Dye 2). ^{1}H NMR (500 MHz, chloroform, δ/ppm): 8.36 (1H, s), 8.30 (1H, s), 8.14−8.07 (4H, d, J = 7.5 Hz), 8.02−7.91 (4H, m), 7.85−7.77 (2H, t), 7.76 (1H, d, J = 7.5 Hz), 7.69−7.63 (2H, dd, J = 7.5, 1.6 Hz), 7.62−7.59 (1H, dd, J = 7.3 Hz), 7.56−7.51 (1H, d, J = 7.2 Hz), 7.48−7.45 (1H, d), 7.37 (2H, t), 7.21−7.19 (2H, d), 6.78 (2H, s), 5.80 (3H, s), 1.33 (18H, s, CH_3); ^{13}CNMR (500 MHz, chloroform, δ/ppm): 147, 144, 143., 142, 141, 138, 138, 135, 131 (2C), 129, 128 (2C), 127, 126 (2C), 125 (4C), 124, 123, 122, 121, 120, 119, 118, 116, 114, 112, 110, 67.03 H (Ar.), 35, 31 (aliphatic). Beige-blue solid, 85% yield.

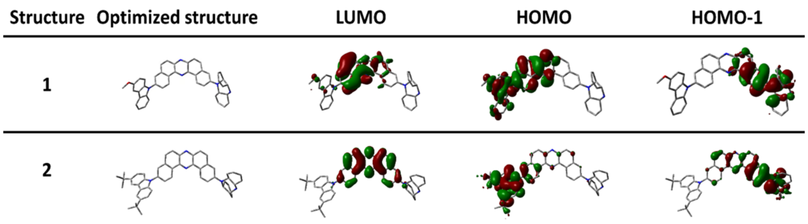

Figure 1. Extracted structure, optimized structures, LUMO, HOMO, and HOMO − 1 distributions from DFT.

Table 1. Extracted Values from DFT and Electrochemical and Photophysical Properties

parameters	dye 1	dye 2
(HOMO/LUMO/E_T) from DFT, eV	(−4.89/−2.44/0.09)	(−5.42/−2.45/0.14)
($E_{\text{onset,-ox}}$/$E_{\text{onset,-red}}$), V	(0.39/−1.70)	(0.40/−1.65)
(E_{CV}^{HOMO}/E_g^{opt} film/EA_{CV}), eV	(−5.19/2.11/3.08)	(−5.20/2.46/2.74)
(T_d/T_g/T_m), °C	(314/83/198)	(326/113/197)
ABS^{max}, nm (toluene/methanol/film)	(219/218/231)	(222/212/216)
PL^{max}, nm (toluene/methanol/film)	(578/603/611)	(543/561/560)
PLQY^{max}, % (toluene/toluene$_{\text{nitrogen ambient}}$/methanol/nondoped film)	(3/5/1/54)	(7/8/6/61)
τ_{PF} spin-coated on the film, ns (77/170/250/300 K)	(14.51/13.15/18.16/13.71)	(15.63/15.93/17.15/19.20)
τ_{DF} spin-coated on the film, ns (77/170/250/300 K)	(5291.08/5952.78/6318.29/6002.19)	(6019.13/6093.05/6366.70/6704.14)
ΔE_{ST} spin-coated on the film, eV	0.03	0.04
PLQY^{max}, % spin-coated dye: (20/40/60/80 wt %) of [Ir(buoppy)$_2$(dmapzpy)] PF$_6$	(56/63/64/71)	(67/68/73/75)

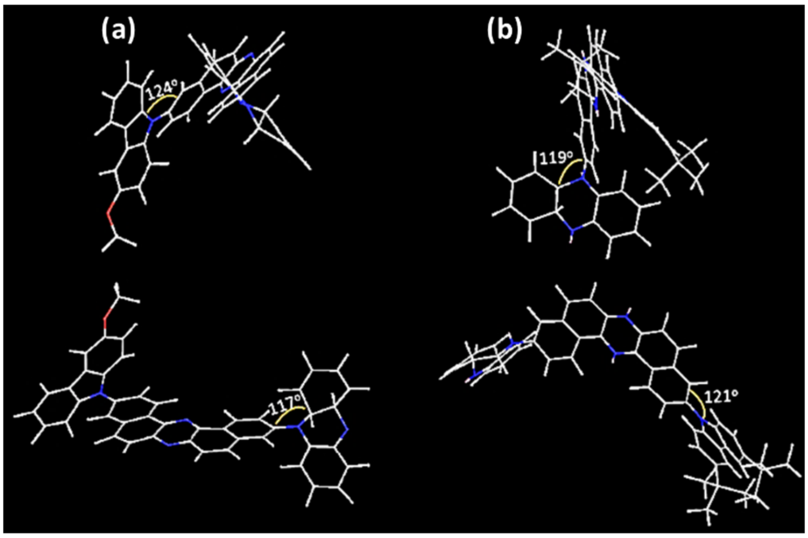

Figure 2. Side views of the single-crystal structures of (a) dye 1 and (b) dye 2.

3. RESULTS AND DISCUSSION

3.1. Synthesis of Dyes

According to the reaction process shown in Scheme 1, the main goal is to perform a nucleophilic reaction and replace the bromine atom with a secondary aromatic amine. This type of reaction was reported by Ullmann using a copper catalyst with a yield of about 80%;[19] however, in this study, a Pd/P(t-Bu)$_3$ catalyst was used, which enables a high-yielding process for coupling secondary aromatic amines with aryl halides. The use of the Pd(OAC)$_2$/P(t-Bu)$_3$ catalyst in this study resulted in a product yield of ~85%, which is a desirable result. Complete purification of the dyestuffs was carried out using column chromatography with a petroleum ether/ethyl acetate mixture. Organic molecules having heterocyclic aromatic rings in the core show good thermal stability, which is enhanced by the addition of arylamine groups. This phenomenon may be due to the inherent asymmetry in the designed chemical structure, which prevents interactions and the formation of unwanted crystals and improves thermal stability.[20]

3.2. TD-DFT Studies

The extracted optimized structures and distributions of the lowest unoccupied molecular orbital (LUMO)−highest occupied molecular orbital (HOMO) from density functional theory (DFT) are shown in Figure 1. The LUMO appears to be delocalized across the central conjugated dibenzo[*a,j*]-phenazine backbone in both molecules, suggesting that the molecule has an extended π-system suitable for charge transfer. Furthermore, in both structures, the HOMO appears to be mainly delocalized over the carbazole and phenazine derivatives, exhibiting asymmetry via the aromatic conjugated system, indicating that the π-electrons from the conjugated

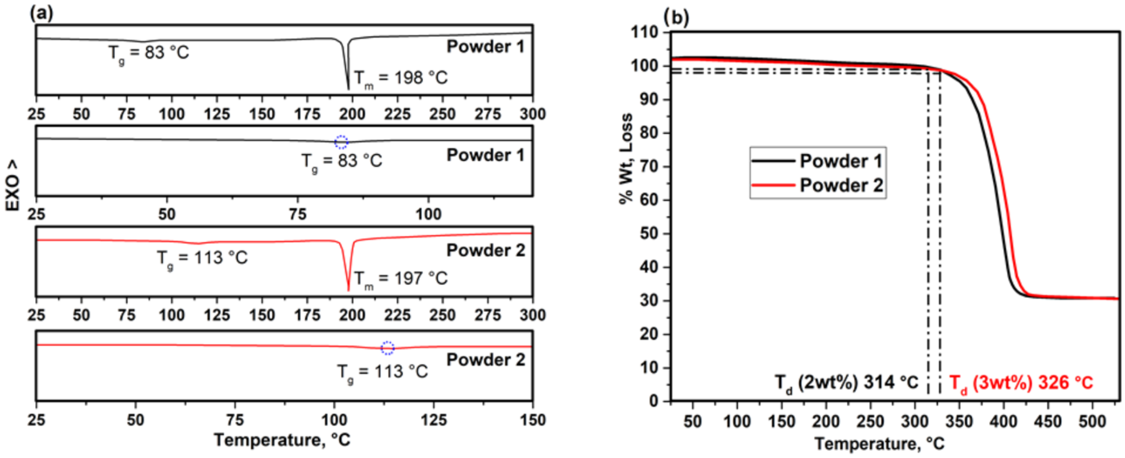

Figure 3. (a) Exo- and endothermic behavior based on DSC curves. (b) TG analysis of the dyes in powder form.

framework. The LUMO−HOMO separation minimizes the overlap of the electron wave function and thus reduces the exchange interaction. This in turn lowers the singlet−triplet energy gap (ΔE_{ST}), which is beneficial for processes such as TADF as it enables efficient exciton utilization.[21,22] In addition, the localization of HOMO − 1 at phenazine ensures that it contributes primarily to the electronic properties of the donor and maintains a clear distinction between donor and acceptor functions.[23] This D−A−D′ design is critical for controlling energy levels and optimizing charge dynamics in optoelectronic devices like LEECs. The LUMO and HOMO values are reported in Table 1, where the electron affinity, which refers to the LUMO values, and the ionization potential, which refers to the HOMO values, are −2.44 and −4.89 eV for the dye consisting of methoxycarbazole and −2.45 and −5.42 eV for the dye consisting of *tert*-butylcarbazole, respectively. The HOMO−LUMO gap for dye 1 is 2.45 eV, and that for dye 2 is 2.97 eV, and these gaps correspond to their emission energy. LEECs with gaps in this range are usually well suited for blue-green or green emission, depending on the excitonic properties. Based on the calculated ΔE_{ST} from the DFT, which are 0.09 and 0.14 eV for dyes 1 and 2, respectively, both dyes are preferred for the TADF mechanism, as these values lead to lower RISC and can ensure a balance between efficient triplet harvesting, contributing to stable LEEC operation; these values are given in refs 24,25.

3.3. Single-Crystal X-ray Diffraction and CV

In Figure 2a,b, the single-crystal XRD data of the dyes show that, from the side view, the angles between the methoxycarbazo/phenazine derivative, as the donor (D)/donor (D′) in tandem, and dibenzo[*a*,*j*]phenazine, as a constant acceptor (A), are evident. To clarify, although dye 1 has a slightly larger bond angle (124° versus 119° for dye 2), this does not directly translate to an overall larger molecular distortion. The larger bond angle for dye 1 reflects a local distortion at a specific site (the methoxycarbazole-phenazine linkage), but overall, dye 2, which contains bulky *tert*-butyl groups, experiences a larger global structural distortion due to steric hindrance. This is reflected in a less compact molecular packing and a more relaxed crystal structure, as confirmed by diffraction analysis (Figure S1). In Figure S1a,c, the close-packed molecules 1 and 2 are shown as triclinic and monoclinic lattices, respectively. In addition, the intermolecular distances (yellow and red lines) indicate specific interactions, such as π-stacking or nitrogen and hydrogen bonding, which are common in molecular crystals. Taking into account the N−N distances, dye 2 exhibits less compact molecular packing due to steric hindrances or increased structural distortions from its bulkier substituent, such as *tert*-butylcarbazole, which allows for a more relaxed packing arrangement, leading to a reduction in aggregation, which is beneficial for optoelectronic devices such as LEECs, as it minimizes exciton quenching and enhances photoluminescence.[26] In addition, dye 2 has a longer π−H distance, which reduces intermolecular interactions and minimizes nonradiative decay pathways, ultimately improving the photoluminescence quantum yield (PLQY).[27] To determine the HOMO and LUMO energy levels of the dyes, cyclic voltammetry (CV) measurements were conducted on the dyes dissolved in dimethylformamide (DMF) (Figure S2). The HOMO energy level $E_{\mathrm{CV}}^{\mathrm{HOMO}}$ was calculated using the following formula: $E_{\mathrm{CV}}^{\mathrm{HOMO}} = [-(E_{\mathrm{onset}}\text{ of oxidation} + 4.8)]$, where the oxidation onset potential is used in the HOMO energy level relative to the vacuum energy level. The oxidation−reduction behavior observed in CV is summarized in Table 1. Notably, the calculated $E_{\mathrm{CV}}^{\mathrm{HOMO}}$ values of the dyes show good agreement with the HOMO energy levels extracted from the DFT calculations. Furthermore, the LUMO energy level is directly related to the electron affinity $[\mathrm{EA}_{\mathrm{CV}} = -(E_{\mathrm{CV}}^{\mathrm{HOMO}} + E_{\mathrm{g}}^{\mathrm{opt}})]$ between the dyes. Dye 2 exhibits a larger optical band gap (2.46 eV) than dye 1 (2.11 eV), suggesting that dye 1 possesses a more extended conjugated system and stronger intramolecular charge transfer. The smaller optical band gap of dyes corresponds to absorption at longer wavelengths (red- or/and blue-shifted), characteristic of materials with enhanced conjugation or charge-transfer properties.

3.4. Investigation of Thermogravimetric (TG) and Differential Scanning Calorimetry (DSC)

The thermal stability of the dyes in powder form is evaluated by TG and DSC diagrams. Both powders exhibit almost similar melting points (198 and 197 °C for dyes 1 and 2 in tandem, respectively), so this factor is less relevant to distinguish their thermal stability, as confirmed in Figure 3a. These melting points are generally sufficient for LEEC fabrication, provided that the dyes also have high thermal decomposition temperatures ($T_{\mathrm{d}} > 300$ °C) and good thermal stability during operation.[28] The extracted values of the thermal properties are given in Table 1. Furthermore, dye 2 exhibits a higher

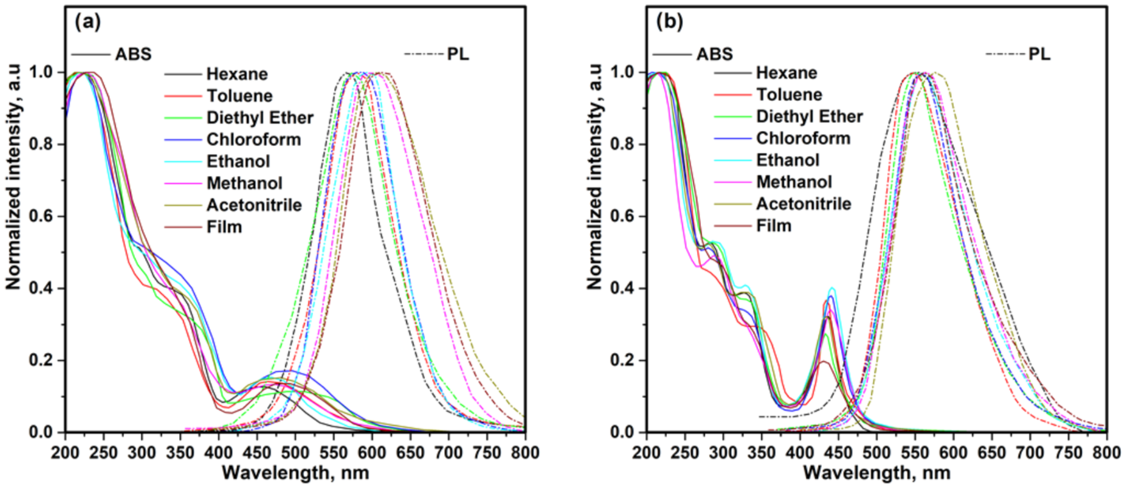

Figure 4. Steady-state UV−vis absorption (Abs) and photoluminescence (PL) spectra of dyes ((a) 1 and (b) 2) in dispersed nonpolar/polar solutions and as solid films.

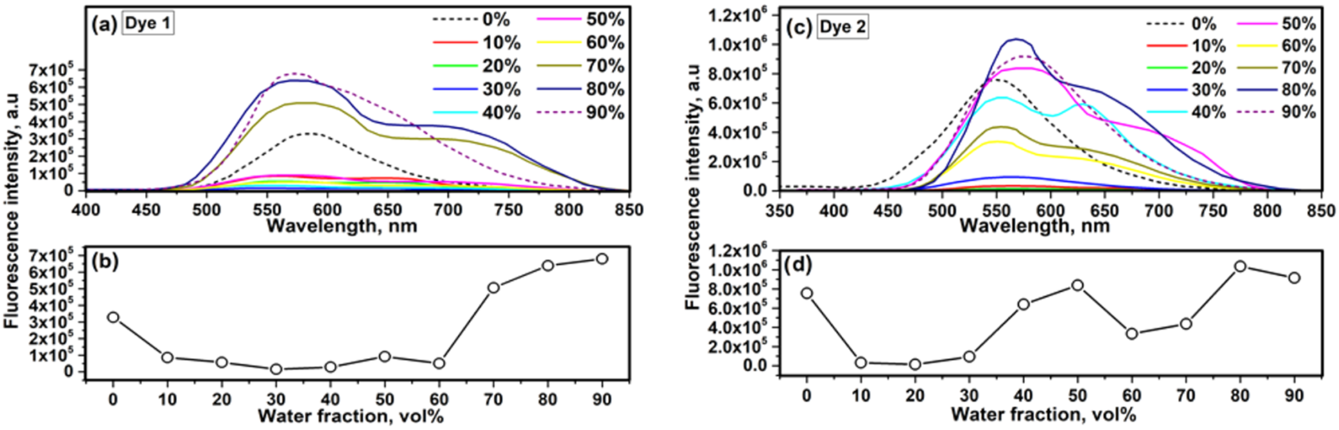

Figure 5. AIEE phenomena: (a, c) PL spectra of the dyes in a water/THF mixture with varying water fractions and (b, d) PL intensity versus water fraction for the dyes.

decomposition temperature, indicating better thermal stability during heating. The glass transition (T_g) values for dyes 1 and 2 are 83 and 113 °C, respectively, showing that powder 2 has higher thermal stability than powder 1, which is related to the more rigid molecular chains in molecule 2, as the rigid structures increase the energy required for the molecular segments to achieve mobility, resulting in a higher T_g.[29] As can be seen, the bulky and thermally robust *tert*-butyl group in dye 2 increases the resistance to decomposition and provides structural rigidity, which contributes to better thermal performance. Moreover, the TG plot in Figure 3b shows the respective decomposition temperatures, with dye 2 showing a loss of 3 wt %, which is slightly more than the loss of powder 1 (2 wt %). However, this difference is small and not as critical as the higher decomposition temperature for determining the overall thermal stability.

3.5. Photophysical Properties

The experimental absorption (ABS) and photoluminescence (PL) spectra of the dyes in different modes are illustrated in Figure 4. To investigate the solvatochromism phenomena, the Stokes shift and polarity function were considered by the following equation: $\Delta f = \frac{\varepsilon - 1}{2\varepsilon + 1} - \frac{n^2 - 1}{2n^2 + 1}$,[30,31] where ε is the dielectric constant and n is the refractive index. The $\Delta \nu$ vs Δf plot is shown in Figure S3. The linear slope of dye 2 (6493) was higher than that of dye 1 (4123), which can be attributed to the presence of a *tert*-butylcarbazole group in the chemical structure of dye 2, which can reduce the planarity of the dye molecule and increase intramolecular distortions during electronic transitions, resulting in larger shifts in energy levels between absorption and emission.[32] A decrease in molecular planarity, as caused by bulky substituents such as the *tert*-butyl groups in dye 2, increases the degree of intramolecular twisting or distortion between donor and acceptor moieties. This geometric relaxation leads to a stronger difference between the geometry of the molecule in the ground state (absorption) and that in the excited state (emission). Particularly, in less planar structures, the molecule undergoes greater structural reorganization during photoexcitation. The excited state adopts a more relaxed, twisted conformation, which stabilizes the lowest excited state and lowers its energy, resulting in a red-shifted emission. However, as absorption occurs from the planar or near-planar ground state, the gap between absorption and emission widens, resulting in a larger Stokes shift. Furthermore, the methoxy group ($-OCH_3$) in dye 1 is an electron-donating group that acts through both inductive and resonance effects. This can stabilize both the ground state and the excited state, leading to a relatively smaller change in the dipole moment and

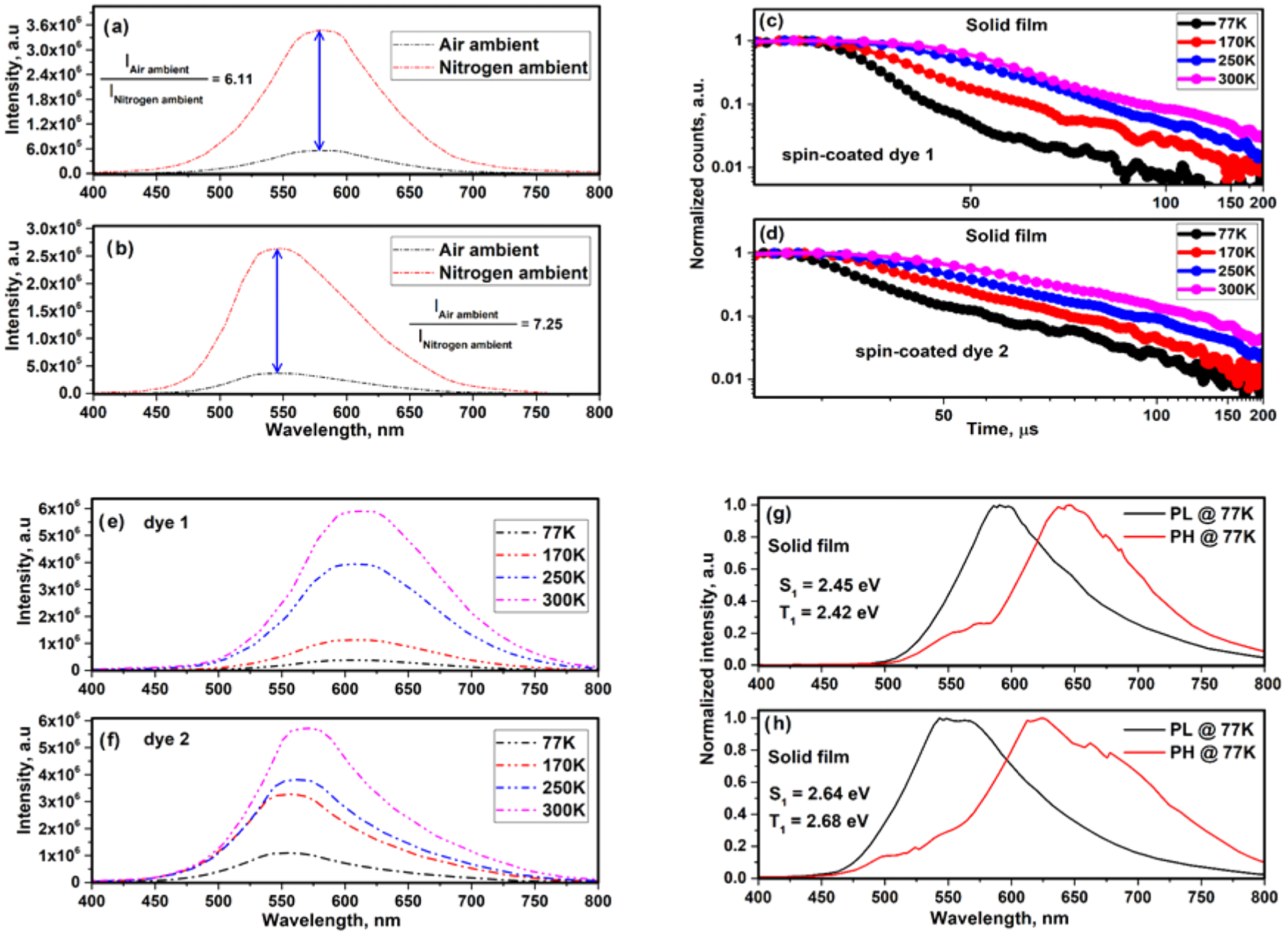

Figure 6. (a, b) PL spectra of dissolved dyes in toluene under air and nitrogen environments, (c, d) PL decay curves of spin-coated dyes on films at different temperatures (77–300 K), (e, f) PL spectra of spin-coated dyes on films at different temperatures (77–300 K), and (g, h) PH spectra of spin-coated dyes on films.

consequently smaller Stokes shift values.[33,34] According to Table 1, the spin-coated dyes on solid films showed reddish-orange and yellowish-green colors when the maximum wavelengths of the absorption spectra were 231 and 216 nm, corresponding to the $\pi-\pi^*$ transitions; additonally, broader and sharper bands at longer wavelengths were attributed to charge transfer (CT), like the intermolecular charge-transfer (ICT) absorption band associated with electron transfer from the carbazole moieties to the dibenzo[*a*,*j*]phenazine moiety.[35]

3.5.1. Investigation of the AIE Mechanism. Aggregation-induced emission enhancement (AIEE) dyes are well suited for LEECs, especially for high-efficiency, solution-processed, and stable devices. Their ability to emit brightly in aggregated states and their tunability make them excellent choices for advanced optical applications. Therefore, AIEE was dominated in this case because the PLQY values of the dispersed dyes in toluene and methanol were lower than those of the nondoped film, and the intensity of the dispersed dyes only in tetrahydrofuran (THF) (0 wt % water) was also not lower than that of other intensities at various water percentages (Figure 5b,d). The PLQYs for dispersed dye 1 in toluene and methanol were 3 and 1%, while for dye 2, the PLQYs were 7 and 6%, calculated in tandem. The higher PLQY of dyes dispersed in toluene than in methanol is primarily due to the nonpolarity of toluene and the absence of hydrogen bonding, which minimizes nonradiative decay pathways. In contrast, the polarity and hydrogen bonds of methanol favor nonradiative relaxation and quenching, which decreases PLQY. The reasons for the occurrence of AIEE phenomena are cited in several references, due to the molecular constraints of intermolecular motion, vibration, and movement.[36−38] It should be noted that in the PL spectra of dispersed dyes, two domains are observed in some of the different water fractions because the polarity of the solvent mixture shifts as the water fraction changes, affecting the solvent−dye interactions. The two domains in the PL spectra arise from the coexistence of monomeric and aggregated dye species, which are influenced by the polarity of the solvent environment, the water fraction, and the aggregation tendencies of the dye.[39] Furthermore, the PL intensity of dispersed dye 2 was higher than that of dye 1 at a water content of 90 wt% (Figure 5a,c), as the presence of bulky and hydrophobic *tert*-butylcarbazole promotes aggregation even at lower water contents due to its poor solubility in polar environments.[40]

3.5.2. Proof and Evaluation of TADF. According to the established rules for TADF dyes, the following criteria were examined for synthesized dyes 1 and 2 to confirm their TADF mechanism:

(1) Enhanced PL intensity in deoxygenated ambient: The PL intensity of the dyes in an oxygen-free environment

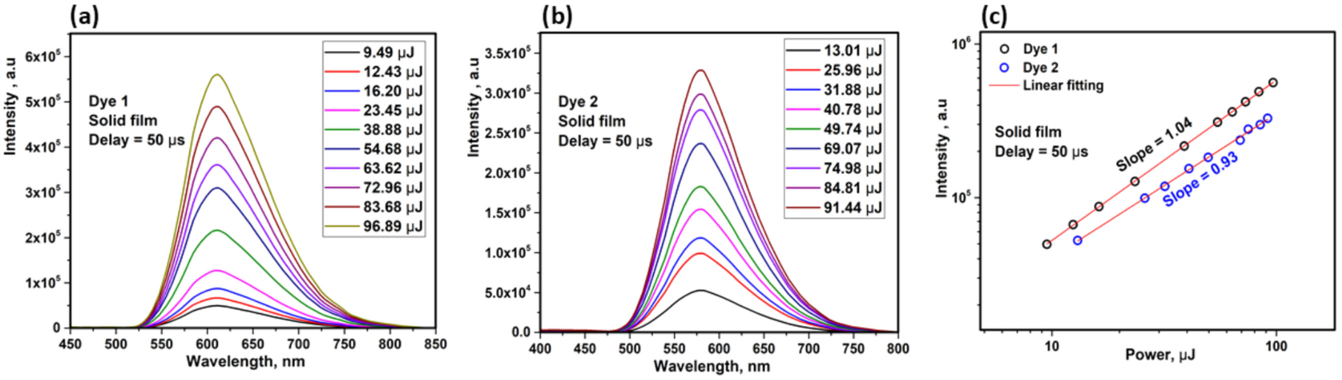

Figure 7. (a, b) Power dependence of the delayed fluorescence of dyes (50 μs) in the solid-state mode and (c) linear fit of the delayed fluorescence intensity of dyes as a function of excitation power.

should be higher than in an oxygenated environment. As shown in Figure 6a,b, the PL spectra of dyes 1 and 2 dispersed in toluene were compared under these two conditions. The intensity ratios were calculated to be 6.11 and 7.25, respectively, which align well with values reported in previous studies.[22,41,42] This enhancement in PL intensity under deoxygenated conditions is due to the absence of collisional quenching, energy transfer to oxygen, and oxidative degradation. Oxygen molecules interact with excited dye molecules in an oxygenated environment, facilitating nonradiative decay pathways and reducing fluorescence intensity.

(2) Temperature-dependent PL intensity and lifetime: The PL intensity and representative lifetime (τ) values of spin-coated dyes on films are lower at low temperatures than at room temperature, as shown in Figure 6c−f and Table 1. This behavior indicates the transition from local excited triplet states (LE^3) to charge-transfer singlet states (CT^1), as the increased PL intensity and lifetime at room temperature support efficient RISC. At low temperatures, energy transfer mechanisms such as Förster resonance energy transfer (FRET) or Dexter energy transfer are hindered due to reduced molecular overlap or exciton trapping, leading to exciton quenching and shorter lifetimes.[43] Additionally, the RISC mechanism is less efficient at low temperatures, causing longer triplet-state lifetimes and increased nonradiative decay.

(3) Small singlet−triplet energy gap (ΔE_{ST}): For efficient RISC, a minimal ΔE_{ST} is critical. The singlet (S_1) and triplet (T_1) energy levels were determined using PL and phosphorescence (PH) spectra measured at 77 K (Figure 6g,h). Based on the onset spectra, the ΔE_{ST} values for spin-coated dyes 1 and 2 were calculated as 0.03 and 0.04 eV, respectively. These values fall within the optimal range for activating RISC and enabling efficient TADF.

(4) Power dependence of delayed fluorescence: The delayed fluorescence intensity should exhibit a sublinear increase with excitation power due to triplet−triplet annihilation (TTA) and RISC saturation at higher excitation powers.[44] To evaluate this, power-dependent measurements were performed on spin-coated dyes on solid films with a constant delay of 50 μs. As shown in Figure 7a,c, increasing laser power flux enhanced the PL intensity. This supports the presence of TADF, as higher excitation power generates more singlet and triplet excitons. The delayed fluorescence depends on RISC, which converts triplet excitons back to the singlet state, thereby enhancing PL intensity with increased power. Figure 7b,d shows intensity versus power, and the slope of the linear fit, which is less than 1, reflects the complex interplay of saturation effects, quenching mechanisms, and triplet-state dynamics that limit the linearity of delayed fluorescence intensity with excitation power; eventually, triplet−triplet annihilation was not observed. As a confirmation, the synthesized dyes 1 and 2 satisfy the key criteria for TADF, as demonstrated by the results from PL intensity comparisons, temperature-dependent measurements, ΔE_{ST} evaluations, and power-dependent delayed fluorescence analyses. These findings confirm that both dyes exhibit a TADF mechanism.[45−49]

3.5.3. Optical Sensing Features of Dyes.

The PL spectra of spin-coated dyes under different atmospheric conditions (air, argon (Ar), and nitrogen) are presented in Figure S4, demonstrating that these molecules exhibit different PL properties depending on the environment. The dyes exhibit remarkable shifts in their PL maxima under different atmospheric conditions, especially between oxygen-containing (air) and inert (Ar, nitrogen) environments, when the maximum wavelengths in air, argon, and nitrogen reached 611, 547, and 540 nm for spin-coated dye 1 and 560, 533, and 555 nm for spin-coated dye 2, respectively. The PL spectrum of molecule 1 shows a more pronounced blue shift in the Ar and nitrogen environments than in air. The blue shift of molecules 1 and 2 is due to the absence of oxygen, which normally quenches higher-energy excited states and stabilizes lower-energy emitting states through interactions such as energy transfer or charge stabilization. Without oxygen, the molecules emit from their intrinsic singlet or triplet states, leading to higher energy (blue-shifted).[50] It is noteworthy that air (containing oxygen) can create a slightly polar environment around the molecules due to the partial charge distribution of oxygen. Polar environments usually stabilize the excited states of the molecule, especially the ICT states, leading to a red shift of the emission. In addition, Ar and nitrogen are nonpolar, inert gases that do not stabilize the excited states in the same way, leading to blue-shifted emissions as the intrinsic energy levels of the excited states dominate.[51]

3.5.4. Doped Spin-Coated Dyes.

In this study, $[Ir(buoppy)_2(dmapzpy)]PF_6$ acted as an efficient phosphorescence host that facilitates Förster or Dexter energy transfer to

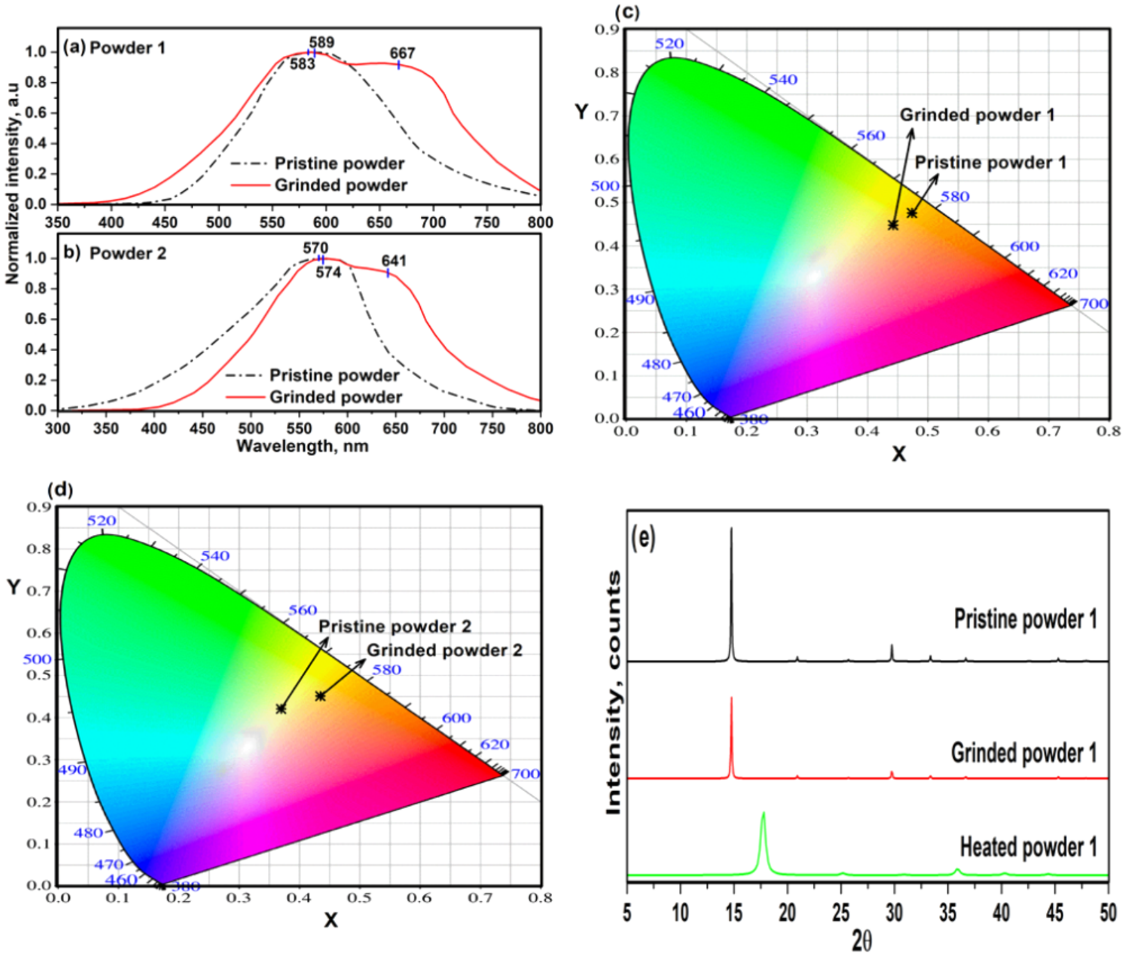

Figure 8. (a, b) PL spectra of stimulated ground dyes; (c, d) C.I.E. chromaticity diagrams of ground dyes; and (e) X-ray diffraction patterns of pristine, ground, and heated dye 1.

dyes 1 and 2, as this energy transfer process helps to occupy the emitting states of the dyes more efficiently. [Ir(buoppy)$_2$(dmapzpy)]PF$_6$ typically has high T$_1$ energy levels (>2.7 eV) due to the ligand design in the molecular structure. The selection of [Ir(buoppy)$_2$(dmapzpy)]PF$_6$ as a host material is based on several considerations. This complex exhibits a high triplet energy level, strong spin−orbit coupling (SOC), and excellent electron transport properties, enabling efficient Förster or Dexter energy transfer to the TADF guest molecules without exciton backtransfer. The use of this complex as a host in this study is noteworthy and crucial, as ionic conductance is important for the operation of LEECs to allow for the formation of dynamic p−i−n junctions during device operation. The PF$_6$ anions present in [Ir(buoppy)$_2$(dmapzpy)]PF$_6$ contribute to the required ionic conductivity and support efficient charge injection and recombination processes. Therefore, [Ir(buoppy)$_2$(dmapzpy)]PF$_6$ not only improves photophysical performance but also fulfills the ionic conductivity requirement specific to LEECs. An organic host alone would not provide the mobile ions required for LEEC operation, and it would have been difficult to simultaneously achieve high triplet energy, efficient charge transport, and ion movement. Therefore, the use of [Ir(buoppy)$_2$(dmapzpy)]PF$_6$ enabled a more comprehensive evaluation of the photophysical properties and device performance of the developed TADF dyes. [Ir(buoppy)$_2$(dmapzpy)]PF$_6$ itself is a very efficient phosphorescent emitter with excellent internal quantum efficiency due to strong SOC. The PLQY value of only [Ir(buoppy)$_2$(dmapzpy)]PF$_6$ as a host on the neat film was calculated to be 83%, which is more than the values of doped dyes reported in this study (Table 1), because it is an intrinsically efficient phosphorescent emitter with minimal nonradiative losses. When doped with TADF dyes, partial energy transfer inefficiencies, additional nonradiative decay pathways introduced by the organic dyes, and slight morphological perturbations in the film contribute to a moderate decrease in the PLQY, which is typical for host−guest systems in LEECs. However, as target materials, doped organic TADF dyes 1 and 2 exhibit more pronounced vibrational and structural relaxation pathways compared to rigid iridium complexes; also, increasing the external quantum efficiency (EQE) of phosphorescent LEECs is complicated because TADF LEECs due to phosphorescence have a high efficiency at low temperatures, but TADF can be considered at room temperature when TADF dyes are cheaper. Furthermore, in pure [Ir(buoppy)$_2$(dmapzpy)]PF$_6$, the PL decay is shorter (Figure S5, τ_{DF} 4729 ns) because the RISC cannot be activated in pure [Ir(buoppy)$_2$(dmapzpy)]PF$_6$ when T$_1$ → S$_0$; however, when doped with TADF dyes 1 and 2, the energy is first transferred from the Ir complex to the dyes. TADF dyes delay the emission by RISC of T$_1$ → S$_1$ → S$_0$ (delayed fluorescence pathway), and the RISC process leads to longer lifetimes of the excited states, although the dyes eventually emit light. The

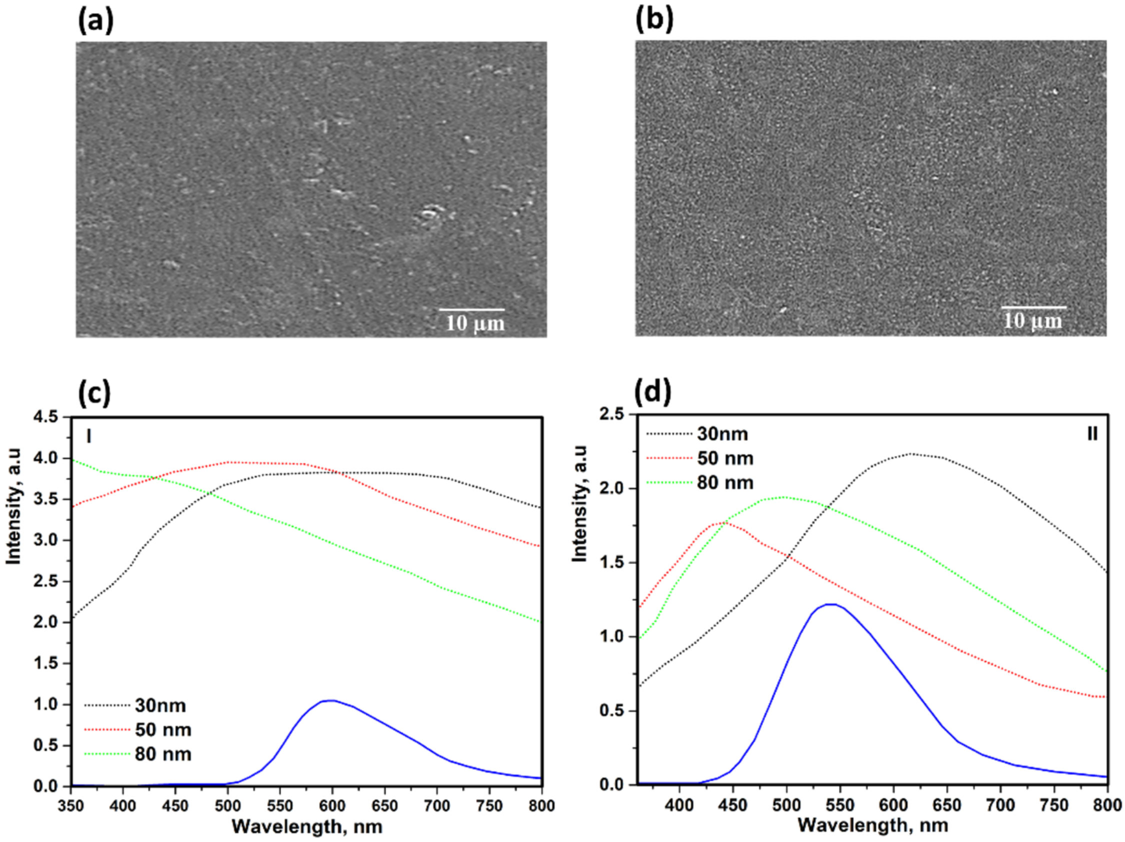

Figure 9. SEM images of (a) ITO/PEDOT:PSS/[Ir(buoppy)$_2$(dmapzpy)]PF$_6$:dye 1 and (b) ITO/PEDOT:PSS/[Ir(buoppy)$_2$(dmapzpy)]PF$_6$:dye 2 and (c, d) $f_{\mathrm{TI}}(\lambda)$ output radiation spectrum of $I(\lambda)$ in the coating of 30, 50, and 80 nm thickness emitting layers.

buoppy and dmapzpy ligands are also engineered to raise the T1 energy level, making this complex an excellent host for energy transfer to lower triplet energy guest emitters, minimizing energy backtransfer and ensuring efficient radiative decay of the guest emitter.[52] The addition of 20−80 wt % Ir [Ir(buoppy)$_2$(dmapzpy)]PF$_6$ to the emitter in solid film mode increased the PLQY values to (56/63/64/71)% and (67/68/73/75)% (Table 1) for doped dyes 1 and 2 in tandem. Furthermore, the [Ir(buoppy)$_2$(dmapzpy)]PF$_6$ complex exhibits high quantum yield and excellent electron transport properties in light-emitting devices. In addition, the [Ir(buoppy)$_2$(dmapzpy)]PF$_6$ complex possesses strong SOC due to the iridium center, which can efficiently harvest T_1 excitons and transfer them to the dyes.[53,54] This enhances the utilization of both S_1 and T_1 excitons, which improves the overall emission efficiency.[55] It is clearly seen that as the content of Ir derivatives increased, two distinct emission regions emerged in the PL spectrum of the doped dyes, except at a certain threshold content of 60 wt % of Ir derivative, as shown in Figure S6. At 60 wt % [Ir(buoppy)$_2$(dmapzpy)]PF$_6$, the host and dye are likely to be in an optimal ratio, allowing efficient Förster or Dexter energy transfer, and the host transfers the energy predominantly to the dye, resulting in a single emission region dominated by the photoluminescence of the dye. Therefore, there is no significant phase separation, and the spectrum shows a single emission peak.

3.6. Mechanoresponsive, Thermoresponsive, and Powder X-ray Diffraction

The PL spectra of the pristine dyes in powder form and ground modes are illustrated in Figure 8a,b. Powder 1 exhibits a color shift from yellow-orange (pristine) to orange (grinded), with additional red emission observed at 667 nm. Similarly, powder 2 shows a shift from yellow (pristine) to yellow-orange (grinded), accompanied by a deep red emission at 641 nm. In the pristine state, molecules 1 and 2 exhibit tighter molecular packing, which leads to specific photophysical properties such as delocalization of excitons. After grinding, the molecular arrangement becomes more disordered, which changes the energy levels and leads to the observed shifts in emission colors. In the crystalline phase, the close packing of the molecules enhances π-conjugation and stabilizes planar conformations, leading to red-shifted emission. However, mechanical forces, such as grinding, lead to changes in the molecular conformation, including torsion or rotation of donor−acceptor groups or π-conjugated segments, disrupting this tight packing and shifting the emission properties. These observations are consistent with previous studies on the effects of mechanical perturbations on photophysical behavior.[56,57] The mechanochromic effect observed in these dyes is due to mechanically induced changes in the molecular arrangement and interactions. This effect is evidenced by the PL spectra and CIE color coordinates, which show significant variations in the luminescence. Furthermore, X-ray diffraction (XRD) patterns of the powder confirm this observation, with pristine powders exhibiting well-defined crystalline lattices. Also, the XRD pattern, consistent with single-crystal XRD analyses, reveal triclinic and monoclinic lattices for dyes 1 and 2, respectively (Figures 8e and S7e). Upon grinding, the XRD patterns indicate a loss of crystallinity, further confirming the mechanically induced structural disorder.[58] In addition, the thermoresponsive behavior of the dyes in powder form was

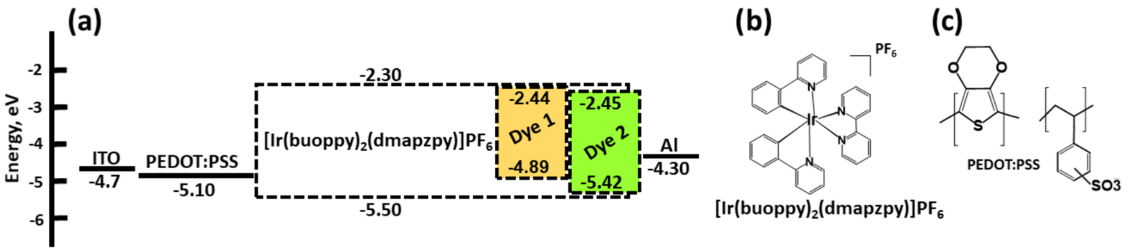

Figure 10. (a) Energy diagram of a typical LEEC layer and chemical structures of (b) [Ir(buoppy)$_2$(dmapzpy)]PF$_6$ and (c) PEDOT:PSS.

also investigated (Figure S7). The PL and XRD results under thermal excitation (Figure S7) demonstrate that heating the powders at 473 K leads to remarkable color changes, with the heated powders exhibiting a predominantly red color, as indicated by the CIE diagrams (Figure S7c,d). The red shift in color is due to changes in molecular arrangement, interactions, and emission states caused by heating. The XRD patterns of the heated powders show broad main peaks, indicating the disruption of weak intermolecular forces such as hydrogen-bonding, $\pi-\pi$ stacking, and van der Waals interactions,[59] which are essential for the maintenance of crystalline order. As these interactions weaken with heat, the molecules lose their ordered packing, leading to broader peaks and an increased level of disorder. In addition, heating leads to mechanical stresses in the molecular lattice, creating defects that disrupt the long-range periodicity detectable in XRD.[60] Overall, the observed mechano- and thermoresponsive effects in these dyes emphasize the significant role of external (mechanical or/and thermal) stimuli in altering molecular packing and photophysical properties. These results provide valuable insights into the structural and emissive behavior of the dyes under varying conditions.

3.7. Study on SEM and Surface Tribology

Based on the tribological study of the surface, Figure 9a,b show~~s~~ scanning electron microscopy (SEM) images of ITO/PEDOT:PSS/[Ir(buoppy)$_2$(dmapzpy)]PF$_6$:dyes as the main component of LEEC device fabrication. Taking this into account, the surface appears to exhibit some notable homogeneities, with visible imperfections or irregularities in small aggregations or uneven distribution, potentially indicating phase separation or incomplete mixing of dye 1 with the PEDOT:PSS matrix. Dye 2 (Figure 9b), on the other hand, shows better integration into the PEDOT:PSS matrix, which could be due to stronger intermolecular interactions or better solubility in the processing solvent. From a photochemical perspective, the reasons are thought to be that methoxy ($-OCH_3$) is a polar functional group that increases the overall polarity of dye 1 and that the polar nature of methoxycarbazole makes it more hydrophilic compared to the bulky, nonpolar *tert*-butylcarbazole (in dye 2).[61] When PEDOT:PSS is processed in polar solvents such as water or alcohol, the hydrophilic methoxy group can favor aggregation due to hydrogen bonding between the methoxy groups or poor dispersion in the hydrophobic PEDOT backbone. Moreover, the methoxy group of dye 1, which exhibits stronger self-aggregation by $\pi-\pi$ stacking between the methoxycarbazole units, can preferentially interact with the PSS chains, leading to phase separation between the dye and the PEDOT backbone, resulting in nonuniform dispersion.[62] In contrast, the *tert*-butyl group of dye 2 interacts more uniformly with the PEDOT:PSS matrix due to the lower polarity mismatch. Figure 9c,d shows the emission spectra of ITO/PEDOT:PSS/[Ir(buoppy)$_2$(dmapzpy)]PF$_6$:dyes for three layer thicknesses (30, 50, and 80 nm). The peak intensity and wavelength shift only minimally, indicating consistent emission properties of the dye across the different thicknesses. $f_{TI}(\lambda)$ is the optical interference that occurs when light emitted within the thin emission layer interacts constructively or destructively due to reflections at the interfaces. $f_{TI}(\lambda)$ is wavelength-dependent and is influenced by the refractive index and thickness of the emitting layer, which change the observed emission intensity profile. The mathematical interpretation based on the equation $f_{TI}(\lambda)$ is as follows: $f_{TI}(\lambda) = 1 + R_1R_2 + 2\sqrt{R_1R_2}\,\cos(\frac{4\pi nd}{\lambda} + \varnothing)$,[63] where R_1 and R_2 are the reflection coefficients at the ITO/PEDOT:PSS/[Ir(buoppy)$_2$(dmapzpy)]PF$_6$:dye interfaces, n is the refractive index of the emitting layer, d is the thickness of the emitting layer (30, 50, 80 nm), λ is the wavelength of the emitted light, ϕ is the phase shift due to the interfaces, and the cosine parameter describes the constructive ($\cos = 1$) or destructive ($\cos = -1$) interference as a function of the optical path length. In addition, the refractive indices of deposited layers were calculated as 1.6 for dye 1 and 1.7 for dye 2 in tandem. In the depth study for dye 1 at 30 nm, the interference factor $f_{TI}(\lambda)$ enhances the emission at certain wavelengths due to constructive interference. This is reflected in the relatively strong intensity over the entire visible range. However, the lower thickness leads to a higher efficiency of radiative recombination due to lower extinction and better charge transport. As the thickness increases, $f_{TI}(\lambda)$ shifts, leading to a reduction in intensity at shorter wavelengths and a broadening of the emission profile.[64] The interference pattern for the 80 nm layer can be less favorable for constructive interference across the spectrum, which reduces the overall intensity. For dye 2, such as dye 1, the 30 nm layer benefits from favorable interference conditions, resulting in a higher emission intensity. The thinner layer also minimizes self-absorption and optical losses. At 50 and 80 nm, the interference factor $f_{TI}(\lambda)$ leads to a redistribution of the intensity over the entire spectrum, with significant shifts in the peak positions. For example, the 80 nm layer shows a reduction in intensity at shorter wavelengths, which is probably due to destructive interference at these wavelengths. Methoxycarbazole (dye 1) shows more stable behavior across the layer thicknesses, while *tert*-butylcarbazole (dye 2) is more affected by interferences, resulting in larger intensity fluctuations and spectral shifts.

3.8. LEEC Fabrication and Electroluminescence Properties

The energy diagrams, in which the energy levels in the different layers of the designed LEECs are arranged, and the molecular structures of [Ir(buoppy)$_2$(dmapzpy)]PF$_6$ and poly(3,4 ethylenedioxythiophene):poly(styrenesulfonate) (PEDOT:PSS) are shown in Figure 10. Indium tin oxide (ITO)

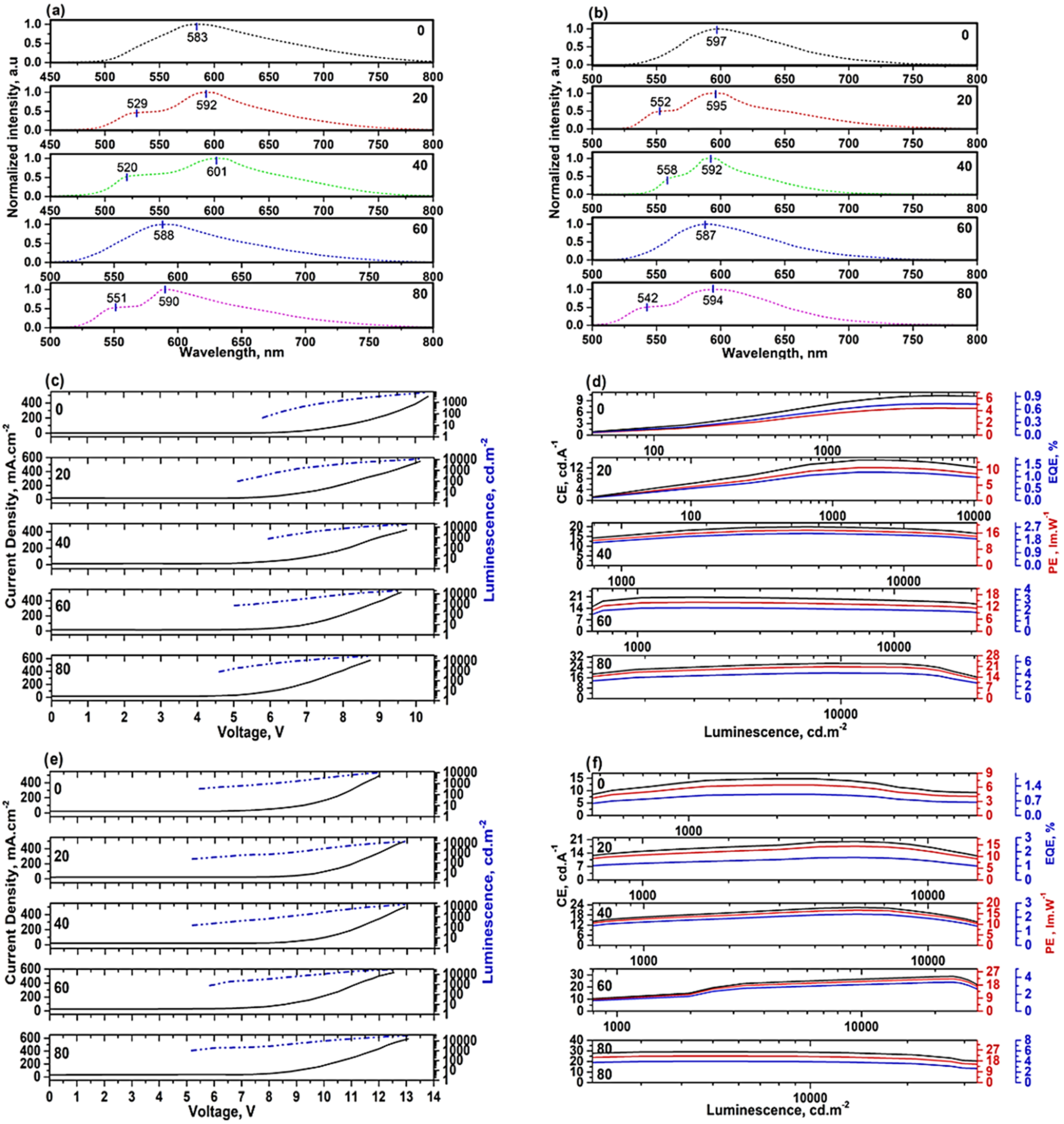

Figure 11. Electroluminescence properties of nondoped and doped devices: (a) EL spectra of devices based on dye 1; (b) EL spectra of devices based on dye 2; (c, e) current density versus voltage plots for devices based on dyes 1 and 2, respectively; and (d, f) CE, PE, and EQE versus luminance plots for devices using dyes 1 and 2 as emitters.

played the role of a hole injector, and PEDOT−PSS is a hole transport layer (HTL), with a work function of −5.10 eV.[65] [Ir(buoppy)$_2$(dmapzpy)]PF$_6$ is an ionic phosphorescent iridium(III) complex host that efficiently harvests both S$_1$ and T$_1$ excitons for light emission, thanks to the strong spin−orbit coupling induced by the iridium center, as the ionic nature of [Ir(buoppy)$_2$(dmapzpy)]PF$_6$ facilitates the formation of p−i−n junctions, which improves the efficiency of charge recombination.[66] Additionally, the selected host material with a high triplet energy level and good charge transport properties can further improve the energy transfer to the dyes and suppress potential exciton losses, as it prevents the backtransfer of recombination to the host.[67,68] Dye 1 exhibits a slightly higher HOMO level, which facilitates electron injection but requires slightly more energy for hole injection from the Al cathode, with a work function of −4.30 eV, which facilitates electron injection into the LUMO of the emitting layer. Accordingly, the energy levels are well matched (PEDOT:PSS, dyes, and Al), which permits a balanced injection of electrons and holes into the active layer.

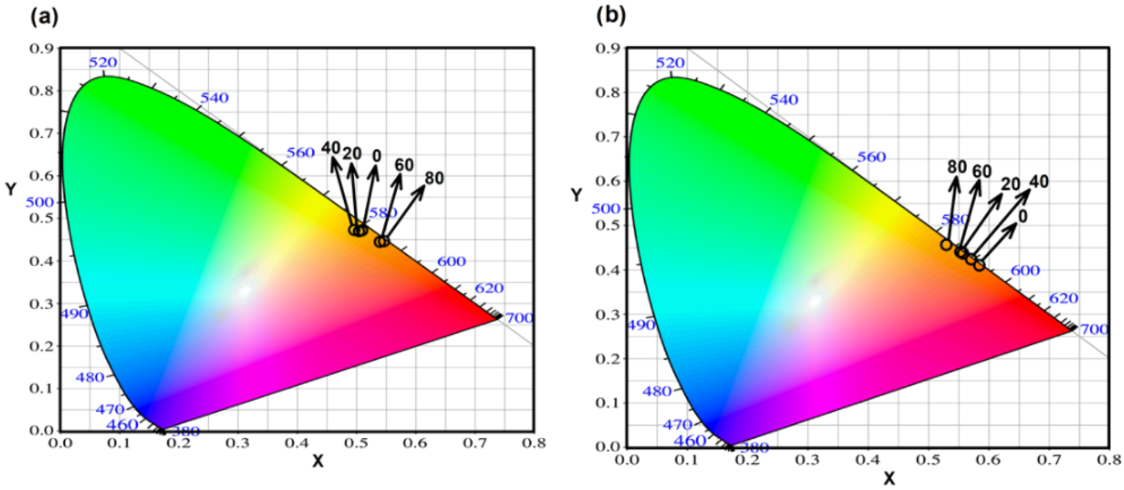

Figure 12. (a, b) C.I.E. chromaticity diagrams of fabricated devices based on dyes 1 and 2 at different weight percentages.

Table 2. Extracted Values from EL Properties of Fabricated Nondoped and Doped LEECs

device	turn-on voltage (V)	maximum brightness $(cd{\cdot}m^{-2})$	maximum current efficiency $(cd{\cdot}A^{-1})$	maximum power efficiency $(lm{\cdot}W^{-1})$	maximum external quantum efficiency (%)	CIE coordinates (X,Y) at 7 V
Based on dye 1						
0	5.80	7420	10.26	4.39	0.73	0.50936, 0.47640
20	5.11	10,864	12.08	8.26	0.95	0.50405, 0.47419
40	5.93	18,383	16.48	14.28	1.86	0.49602, 0.47723
60	5.02	21,361	16.27	11.14	1.76	0.53944, 0.44974
80	4.61	31,010	16.16	12.46	2.49	0.54623, 0.45091
Based on dye 2						
0	5.42	9756	14.80	6.48	1.00	0.58402, 0.41502
20	5.15	15,027	20.05	14.32	1.59	0.55267, 0.44552
40	5.13	15,080	22.33	16.25	2.21	0.57048, 0.42855
60	5.80	30,055	28.78	22.13	3.42	0.55675, 0.44166
80	5.16	32,935	28.97	22.11	4.02	0.52953, 0.46104

In Figure 11a,b, the electroluminescence (EL) spectrum of nondoped and doped LEECs shows that increasing the content of $[Ir(buoppy)_2(dmapzpy)]PF_6$ as a host affects the maximum peak wavelengths impressively and the color of the devices rarely when the CIE color investigate coordinates in Figure 12 showed the exact color point to point. Interestingly, in both packages of devices based on either dye 1 or dye 2 as the emitter, the EL spectrum of the nondoped devices exhibited maximum wavelength of yellow color, and the EL spectrum above 28 nm showed a blue shift relative to the PL spectra of spin-coated dyes on films; this effect was more profound for dye 2, where the red-shifted spectrum dominated the PL spectrum. The reason for this is that the blue shift of the EL spectrum compared to the PL spectrum of thin films is due to the suppression of aggregation and emission mainly from the monomeric states under charge recombination conditions. In contrast, red shifts in EL spectra for dye 2 occur when aggregated states, excimers, or CT states dominate, which are influenced by molecular packing, film morphology, or thicker layers. The interplay of these effects makes EL tuning particularly interesting and highlights the importance of optimizing device architecture so that PEDOT:PSS and Al have a greater influence on recombination in the emitter layer. Taking into account the increasing content of the iridium complex as a host, two maximum wavelengths appear as domains in the PL spectra (Figure S6); however, at the optimal value of 60 wt % $[Ir(buoppy)_2(dmapzpy)]PF_6$, single emission peaks at 588 and 587 nm were observed for both categories of LEECs due to the optimal efficiency of energy transfer between the host and guest; at this concentration, the Forster−Dexter energy transfer is complete and the iridium complex efficiently transfers energy to the guest, resulting in dominant emission from the guest.[69] At suboptimal host concentrations (20, 40, and 80 wt %), there is incomplete energy transfer or excessive emission from the host, which leads to double peaks. According to Figure 11c,e and the tabulated values of EL characteristics in Table 2, the lowest turn-on voltage was recorded for doped devices based on 80 wt % host:dye 1 and 40 wt % host:dye 2, respectively, when the voltages were 4.61 and 5.13 V in tandem. It is clear that dye 1, which consists of methoxycarbazole as the D moiety and is doped in 80 wt % host, exhibits better charge injection and charge transport, resulting in the lowest turn-on voltage (4.61 V). In addition, the device based on dye 2, which consists of *tert*-butylcarbazole with 40 wt % host, is more dependent on the guest for emission, resulting in a higher turn-on voltage (5.13 V). In addition, a higher iridium content improves radiative recombination, suppresses nonradiative losses, and increases exciton harvesting, resulting in brightness values above 31,010 and 32,935 cd/m^2 for devices based on dyes 1 and 2 as emitters, respectively. It can be demonstrated that at 80 wt % host, the balance between host charge transport and guest emission efficiency was optimized. Furthermore, the substitution of *tert*-butylcarbazole in dye 2 played an important role. This group in the chemical structure prevented molecular aggregation, reduced nonradiative decay pathways, and led to enhanced molecular dispersion in the host matrix, which improved energy transfer efficiency and emission. The plots of current efficiency (CE), power efficiency (PE), and EQE versus luminescence (L) are shown in Figure 11d,f. From the extracted values, the fabricated devices based on 80 wt % host:dye 2 demonstrated better quality and more reduced exciton quenching with a higher proportion of radiative recombination, increasing the CE, PE, and EQE values, which achieved 28.97 cd·A^{-1}, 22.11 lm·W^{-1}, and 4.02%, respectively. The PLQY is directly proportional to EQE, as a higher PLQY means that a greater proportion of excitons contribute to light emission rather than being lost to nonradiative decay. As expected, high PLQYs indicate efficient radiative recombination, meaning that a larger fraction of excitons contributes to light emission, as shown by the calculated PLQYs (Table 1), with the doped film of *tert*-butylcarbazole exhibiting the highest value of 75%. The methoxycarbazole substitution has been shown to lack such a bulky substituent, making it more prone to aggregation, resulting in nonradiative losses and lower EQEs for devices based on 80 wt % host.

4. CONCLUSIONS

Two mechanochromic and thermochromic TADF molecules based on phenazine derivatives substituted with *tert*-butylcarbazole and methoxycarbazole were successfully synthesized and characterized. The substituents significantly influenced the electronic properties, with calculated HOMO/LUMO values of −4.89/−2.44 eV for the methoxycarbazole dye and −5.42/−2.45 eV for the *tert*-butylcarbazole dye, in agreement with experimental EA_{CV} values (3.08 and 2.74 eV, respectively). Notably, dye 2 demonstrated superior thermal stability (T_g = 113 °C) compared to dye 1 (T_g = 83 °C), which is attributed to its more rigid molecular structure, confirming the effectiveness of the design strategy for enhancing material robustness. Furthermore, dye 2 exhibited higher PL intensity in water (90 wt %) than dye 1, which can be attributed to the bulky and hydrophobic *tert*-butylcarbazole that promotes aggregation at lower water contents. The dyes displayed TADF behavior, as (1) the PL intensity of the dispersed dyes in toluene increased upon oxygen deprivation, (2) small ΔE_{ST} values were recorded to be 0.03 and 0.04 eV for spin-coated dyes 1 and 2 on the solid films in tandem, (3) the lifetime values from PL decay were higher at room temperature than at lower temperatures, and (4) the slope of less than 1 of the linear fit of intensity versus power ignored any claims of triplet−triplet annihilation phenomena. As a result, both dyes exhibited significant shifts in their PL maxima under different atmospheric conditions, suggesting a sensing behavior. Also, in this study, $[Ir(buoppy)_2(dmapzpy)]PF_6$ acted as an efficient host with strong phosphorescence, which facilitated Förster or/and Dexter energy transfer to the dyes. Incorporation of 20−80 wt % host into solid-state emitters increased PLQY values, reaching 56−71% for dye 1 and 67−75% for dye 2. The host substance also demonstrated electron transport properties, making it suitable for use in light-emitting devices. Both dyes showed color shifts during grinding: dye 1 shifted from yellow-orange (pristine) to orange (after grinding), while dye 2 shifted from yellow (pristine) to yellow-orange (after grinding) with deep red emission. In addition, the XRD patterns of the heated dyes in powder mode revealed broad peaks, indicating the disruption of weak intermolecular interactions such as hydrogen-bonding, π−π stacking, and van der Waals forces. The emission spectra of ITO/PEDOT:PSS/$[Ir(buoppy)_2(dmapzpy)]PF_6$:dyes showed minimal shifts across different layer thicknesses. The EL spectra of the LEECs showed that an optimized iridium complex host fraction (60 wt %) enabled efficient Förster or/and Dexter energy transfer, resulting in single emission peaks for both dyes. Devices doped with 80 wt % host exhibited improved charge injection, lower nonradiative losses, and high brightness (31,010 cd/m^2 for dye 1 and 32,935 cd/m^2 for dye 2), along with better CE (28.97 cd·A^{-1}), PE (22.11 lm·W^{-1}), and EQE (4.02%) values for dye 2. The bulky *tert*-butylcarbazole substitution in dye 2 reduced aggregation, improved molecular dispersion, and achieved high PLQY (75%) in doped mode, resulting in better overall device performance compared to methoxycarbazole-based devices.

■ ASSOCIATED CONTENT

Supporting Information

The Supporting Information is available free of charge at https://pubs.acs.org/doi/10.1021/acsaom.5c00065.

Synthesis, single-crystal X-ray data, and photophysical characterization of dyes 1 and 2 (PDF)

■ AUTHOR INFORMATION

Corresponding Authors

Marzieh Rabiei − *Department of Mechanical, Energy and Biotechnology Engineering, Vytautas Magnus University, LT-53361 Kaunor, Lithuania*; Email: rabieimarzieh7@gmail.com

Sohrab Nasiri − *Department of Mechanical, Energy and Biotechnology Engineering, Vytautas Magnus University, LT-53361 Kaunor, Lithuania; Faculty of Mechanical Engineering and Design, Kaunas University of Technology, LT-51373 Kaunas, Lithuania; Department of Chemistry, Queens University, Kingston, Ontario K7L 3N6, Canada*; orcid.org/0000-0002-5574-3675; Email: sohrab.nasiri2017@gmail.com

Authors

Mozhgan Hosseinnezhad − *Department of Organic Colorants, Institute for Color Science and Technology, P.O. Box 16656118481 Tehran, Iran*; orcid.org/0000-0003-3351-0157

Raheleh Ghahary − *Department of Chemistry, Najafabad Branch, Islamic Azad University, Najafabad 85141-43131, Iran*

Venkatramaiah Nutalapati − *Department of Chemistry, Faculty of Engineering and Technology, SRM Institute of Science and Technology, Kattankulathur 603203 Tamil Nadu, India*; orcid.org/0000-0003-0235-2707

Jean-Michel Nunzi − *Department of Physics, Engineering Physics & Astronomy and Department of Chemistry, Queens University, Kingston, Ontario K7L 3N6, Canada*; orcid.org/0000-0001-5490-4273

Juozas Padgurskas − *Department of Mechanical, Energy and Biotechnology Engineering, Vytautas Magnus University, LT-53361 Kaunor, Lithuania*; orcid.org/0000-0003-1275-9105

Raimundas Rukuiza − *Department of Mechanical, Energy and Biotechnology Engineering, Vytautas Magnus University, LT-53361 Kaunor, Lithuania*

Complete contact information is available at:
https://pubs.acs.org/10.1021/acsaom.5c00065

Author Contributions

M.R.: conceptualization, methodology, and writing-original draft. M.H.: methodology and investigation. R.G.: photophysical investigation. V.N.: methodology and single-crystal X-ray diffraction. S.N.: validation, writing-review and editing. J.-M.N.: writing-review and editing. J.P.: writing-review and supervision. R.R.: editing, supervision, and resources

Notes

The authors declare no competing financial interest.

■ ACKNOWLEDGMENTS

This project has received funding from the Research Council of Lithuania (LMTLT), agreement no. S-PD-24-82.

■ REFERENCES

(1) Meier, S. B.; Tordera, D.; Pertegás, A.; Roldán-Carmona, C.; Ortí, E.; Bolink, H. J. Light-Emitting Electrochemical Cells: Recent Progress and Future Prospects. *Mater. Today* **2014**, *17* (5), 217−223.

(2) Pei, Q.; Yang, Y.; Yu, G.; Zhang, C.; Heeger, A. J. Polymer Light-Emitting Electrochemical Cells: In Situ Formation of a Light-Emitting p-n Junction. *J. Am. Chem. Soc.* **1996**, *118* (16), 3922−3929.

(3) Costa, R. D.; Ortí, E.; Bolink, H. J.; Monti, F.; Accorsi, G.; Armaroli, N. Luminescent Ionic Transition-Metal Complexes for Light-Emitting Electrochemical Cells. *Angew. Chem., Int. Ed.* **2012**, *51* (33), 8178−8211.

(4) Gao, J. Strategies toward Long-Life Light-Emitting Electrochemical Cells. *ChemPlusChem* **2018**, *83* (4), 183−196.

(5) Yersin, H. *Highly Efficient OLEDs*; Yersin, H., Ed.; Wiley-VCH Verlag GmbH & Co. KGaA: Weinheim, Germany, 2018.

(6) Sanz-Rodrigo, J.; Olivier, Y.; Sancho-García, J. C. Computational Studies of Molecular Materials for Unconventional Energy Conversion: The Challenge of Light Emission by Thermally Activated Delayed Fluorescence. *Molecules* **2020**, *25* (4), 1006.

(7) Zhang, T.; Xiao, Y.; Wang, H.; Kong, S.; Huang, R.; Ka-Man Au, V.; Yu, T.; Huang, W. Highly Twisted Thermally Activated Delayed Fluorescence (TADF) Molecules and Their Applications in Organic Light-Emitting Diodes (OLEDs). *Angew. Chem., Int. Ed.* **2023**, *62* (39), No. e202301896.

(8) Berberan-Santos, M. N.; Garcia, J. M. M. Unusually Strong Delayed Fluorescence of C70. *J. Am. Chem. Soc.* **1996**, *118* (39), 9391−9394.

(9) Farokhi, A.; Lipinski, S.; Cavinato, L. M.; Shahroosvand, H.; Pashaei, B.; Karimi, S.; Bellani, S.; Bonaccorso, F.; Costa, R. D. Metal Complex-Based TADF: Design, Characterization, and Lighting Devices. *Chem. Soc. Rev.* **2025**, *54* (1), 266−340.

(10) Barman, D.; Gogoi, R.; Narang, K.; Iyer, P. K. Recent Developments on Multi-Functional Metal-Free Mechanochromic Luminescence and Thermally Activated Delayed Fluorescence Organic Materials. *Front. Chem.* **2020**, *8*, No. 531643.

(11) Sagara, Y.; Yamane, S.; Mitani, M.; Weder, C.; Kato, T. Mechanoresponsive Luminescent Molecular Assemblies: An Emerging Class of Materials. *Adv. Mater.* **2016**, *28* (6), 1073−1095.

(12) Nasiri, S.; Hosseinnezhad, M.; Rabiei, M.; Palevicius, A.; Rahimi, Z.; Janusas, G.; Vilkauskas, A. New Approach of Mechanochromic, Thermally Activated Delayed Fluorescence' Dyes Consisting of "Thioxanthenone Derivative as an Acceptor Unit and Two Carbazole Derivatives as the Donor Units" Used as Emitting Layer in Organic Light-Emitting Diodes. *Opt. Mater.* **2022**, *127*, No. 112320.

(13) Chen, M.; Chen, Y.; Su, Z.; Li, Y.; Fei, H.; Zhang, H.; Wu, Y. Achievement of Efficient Thermally Activated Delayed Fluorescence Materials Based on 1,8-Naphthalimide Derivatives Exhibiting Piezochromic and Thermochromic Luminescence. *RSC Adv.* **2024**, *14* (25), 17434−17439.

(14) Ansari, R.; Shao, W.; Yoon, S.-J.; Kim, J.; Kieffer, J. Charge Transfer as the Key Parameter Affecting Color Purity of TADF Emitters, 2021.

(15) Bas, E. E.; Ulukan, P.; Monari, A.; Aviyente, V.; Catak, S. Photophysical Properties of Benzophenone-Based TADF Emitters in Relation to Their Molecular Structure. *J. Phys. Chem. A* **2022**, *126* (4), 473−484.

(16) Hong, G.; Si, C.; Gupta, A. K.; Bizzarri, C.; Nieger, M.; Samuel, I. D. W.; Zysman-Colman, E.; Bräse, S. Fluorinated Dibenzo[a,c]-Phenazine-Based Green to Red Thermally Activated Delayed Fluorescent OLED Emitters. *J. Mater. Chem. C* **2022**, *10* (12), 4757−4766.

(17) Zhao, T.; Jiang, S.; Tao, X. D.; Yang, M.; Meng, L.; Chen, X. L.; Lu, C. Z. Dihydrophenazine-Derived Thermally Activated Delayed Fluorescence Emitters for Highly Efficient Orange and Red Organic Light-Emitting Diodes. *Dyes Pigm.* **2023**, *211*, No. 111065.

(18) Okazaki, M.; Takeda, Y.; Data, P.; Pander, P.; Higginbotham, H.; Monkman, A. P.; Minakata, S. Thermally Activated Delayed Fluorescent Phenothiazine−Dibenzo[a,j]Phenazine−Phenothiazine Triads Exhibiting Tricolor-Changing Mechanochromic Luminescence. *Chem. Sci.* **2017**, *8* (4), 2677−2686.

(19) Paine, A. J. Mechanisms and Models for Copper Mediated Nucleophilic Aromatic Substitution: 2: A Single Catalytic Species from Three Different Oxidation States of Copper in an Ullmann Synthesis of Triarylamines1. *J. Am. Chem. Soc.* **1987**, *109* (5), 1496−1502.

(20) Hosseinnezhad, M.; Nasiri, S.; Nutalapati, V.; Gharanjig, K.; Arabi, A. M. A Review of the Application of Organic Dyes Based on Naphthalimide in Optical and Electrical Devices. *Prog. Color Colorants Coat.* **2024**, *17*, 417−433, DOI: 10.30509/PCCC.2024.167247.1267.

(21) Wazzan, N. A. A DFT/TDDFT Investigation on the Efficiency of Novel Dyes with Ortho-Fluorophenyl Units (A1) and Incorporating Benzotriazole/ Benzothiadiazole/Phthalimide Units (A2) as Organic Photosensitizers with D-A2-*π*-A1 Configuration for Solar Cell Applications. *J. Comput. Electron.* **2019**, *18*, 375−395.

(22) Nasiri, S.; Rabiei, M.; Shaki, H.; Hosseinnezhad, M.; Kalyani, K.; Palevicius, A.; Vilkauskas, A.; Janusas, G.; Nutalapati, V.; Kment, S.; Michel Nunzi, J. What Is TADF (Thermally Activated Delayed Fluorescence) Compared to the Mechanisms of FL (Fluorescence), PH (Phosphorescence), and TTA (Triplet−Triplet Annihilation) Based on a Novel Naphthalimide Sulfonylphenyl Derivative as a Host? *J. Photochem. Photobiol. A* **2024**, *447*, No. 115289.

(23) Ren, Z.; Zhang, B.; Yang, Y.; Zhu, Y.; Zhao, J.; Zhao, Z. Molecular Orbital Tomography of HOMO and HOMO-1 of the Nonlinear Molecule H2O: The Study on Multi-Orbital Effects. *Results Phys.* **2023**, *55*, No. 107181.

(24) Choi, M. G.; Lee, C. H.; Adachi, C.; Lee, S. Y. Highly Effective Thermally Activated Delayed Fluorescence Emitters Based on Symmetry and Asymmetry Nicotinonitrile Derivatives. *Molecules* **2022**, *27* (23), 8274.

(25) Leng, J.; Zhang, Z.; Zhang, Y.; Sun, J.; Ma, H. Excited State Properties of Two Unusual Thermally Activated Delayed Fluorescence Molecules: A Theoretical Investigation. *J. Lumin.* **2018**, *204*, 312−318.

(26) Zhou, N.; Lu, Y.; Zhou, J.; Xu, D.; Jia, Q.; Liu, X. Carbazole-Modified Dicyanoethylene Derivatives Exhibiting Tert-Butyl-Regulated Aggregation-Induced Emission and Reversible High-Contrast Mechanofluorochromism. *J. Lumin.* **2024**, *266*, No. 120332.

(27) Pandey, S. K. Computational Study on the Structure, Stability, and Electronic Feature Analyses of Trapped Halocarbons inside a Novel Bispyrazole Organic Molecular Cage. *ACS Omega* **2021**, *6* (17), 11711−11728.

(28) Tyagi, P.; Srivastava, R.; Giri, L. I.; Tuli, S.; Lee, C. Degradation of Organic Light Emitting Diode: Heat Related Issues and Solutions. *Synth. Met.* **2016**, *216*, 40−50.

(29) Jayakumar, J.; Wu, W. L.; Chang, C. L.; Han, T. Y.; Ting, L. Y.; Yeh, C. M.; Hung, H. W.; Chou, H. H. Highly Thermal Stable

Electron-Transporting Materials Using Triptycene Derivatives for OLEDs. *Org. Electron.* **2021**, *88*, No. 106013.

(30) Mohd Yusof Chan, N. N.; Idris, A.; Zainal Abidin, Z. H.; Tajuddin, H. A.; Abdullah, Z. Intramolecular Charge Transfer-Induced Solvatochromism and Large Stokes Shifts of Furocoumarins. *Mater. Chem. Phys.* **2022**, *276*, No. 125406.

(31) Qiu, S.; Yu, J.; Zhou, T.; Zhang, K.; Duan, Y.; Ban, X.; Zhu, Q.; Shi, L.; Zhang, D. Thermally Activated Delayed Fluorescence Fluorescent Probe Based on Triazine as Emission Core for Metal Ions Detection. *Opt. Mater.* **2021**, *119*, No. 111303.

(32) Stanimirov, S.; Djumayska, S.; Todorova, N.; Mutovska, M.; Konstantinov, K.; Petrova, P.; Tomova, R.; Ivanov, P.; Ivanova, G.; Stoyanov, S.; Spassov, T.; Trifonov, A.; Buchvarov, I.; Baumgarten, M.; Ivanova, A.; Zagranyarski, Y. TADF Blue Emitters with Balanced *π*-Conjugation – Design, Synthesis, Spectral Characterization, and a Model OLED with 8-(5-(Tert-Butyl)-1,3,4-Oxadiazol-2-Yl)-N,N-Bis-(4-(Tert-Butyl)Phenyl)Dibenzo[b,d]Furan-2-Amine. *J. Phys. Chem. A* **2024**, *128* (26), 5100−5114.

(33) Wazzan, N.; Safi, Z. Effect of Number and Position of Methoxy Substituents on Fine-Tuning the Electronic Structures and Photophysical Properties of Designed Carbazole-Based Hole-Transporting Materials for Perovskite Solar Cells: DFT Calculations. *Arab. J. Chem.* **2019**, *12* (1), 1−20.

(34) Staderini, M.; Vanni, S.; Baldeschi, A. C.; Giachin, G.; Zattoni, M.; Celauro, L.; Ferracin, C.; Bistaffa, E.; Moda, F.; Pérez, D. I.; Martínez, A.; Martín, M. A.; Martín-Cámara, O.; Cores, Á.; Bianchini, G.; Kammerer, R.; Menéndez, J. C.; Legname, G.; Bolognesi, M. L. Bifunctional Carbazole Derivatives for Simultaneous Therapy and Fluorescence Imaging in Prion Disease Murine Cell Models. *Eur. J. Med. Chem.* **2023**, *245*, No. 114923.

(35) Rouhani, S.; Hosseinnezhad, M.; Sohrab, N.; Gharanjig, K.; Salem, A.; Ranjbar, Z. Investigation of the Effect of RGO/TiO2 on Photovoltaic Performance of DSSCs Devices. *Prog. Color Colorants Coatings* **2022**, *15* (2), 123−131.

(36) Suman, G. R.; Pandey, M.; Chakravarthy, A. S. J. Review on New Horizons of Aggregation Induced Emission: From Design to Development. *Mater. Chem. Front.* **2021**, *5* (4), 1541−1584.

(37) Liu, D.; Wei, J. Y.; Tian, W. W.; Jiang, W.; Sun, Y. M.; Zhao, Z.; Tang, B. Z. Endowing TADF Luminophors with AIE Properties through Adjusting Flexible Dendrons for Highly Efficient Solution-Processed Nondoped OLEDs. *Chem. Sci.* **2020**, *11* (27), 7194−7203.

(38) Tang, H.; Gao, J.; Zhang, L.; Li, X.; Duan, Y. C.; Wen, L.; Liu, X.; Su, Z. M. A Theoretical Study and Design of AIE-Type TADF Materials Derived from Spatially Conjugated [2.2]Paracyclophane. *New J. Chem.* **2024**, *48* (47), 19811−19818.

(39) Dutt, S.; Urkude, R.; Singh, S. D.; Sagdeo, A. Unveiling the Origin of Multiple Peak Emission in Derivative Perovskite Single Crystals, CH3NH3Pb(Br1−xClx)3 (x = 0−1). *J. Appl. Phys.* **2024**, *136* (19), No. 195501.

(40) Knötig, K. M.; Gust, D.; Oum, K.; Lenzer, T. Excited-State Dynamics of Carbazole and Tert-Butyl-Carbazole in Thin Films. *Photochem* **2024**, *4* (2), 179−197.

(41) Ni, F.; Zhu, Z.; Tong, X.; Zeng, W.; An, K.; Wei, D.; Gong, S.; Zhao, Q.; Zhou, X.; Yang, C. Hydrophilic, Red-Emitting, and Thermally Activated Delayed Fluorescence Emitter for Time-Resolved Luminescence Imaging by Mitochondrion-Induced Aggregation in Living Cells. *Adv. Sci.* **2019**, *6* (5), No. 1801729.

(42) Zhang, Y.; Ma, H.; Wang, S.; Li, Z.; Ye, K.; Zhang, J.; Liu, Y.; Peng, Q.; Wang, Y. Supramolecular Structure-Dependent Thermally-Activated Delayed Fluorescence (TADF) Properties of Organic Polymorphs. *J. Phys. Chem. C* **2016**, *120* (35), 19759−19767.

(43) Haase, N.; Danos, A.; Pflumm, C.; Stachelek, P.; Brütting, W.; Monkman, A. P. Are the Rates of Dexter Transfer in TADF Hyperfluorescence Systems Optically Accessible? *Mater. Horiz.* **2021**, *8* (6), 1805−1815.

(44) Zhang, M.; Wang, K.; Zheng, C. J.; Wang, D. Q.; Shi, Y. Z.; Lin, H.; Tao, S. L.; Li, X.; Zhang, X. H. Development of Red Exciplex for Efficient OLEDs by Employing a Phosphor as a Component. *Front. Chem.* **2019**, *7*, No. 435512.

(45) Hong, X.; Zhang, D.; Yin, C.; Wang, Q.; Zhang, Y.; Huang, T.; Wei, J.; Zeng, X.; Meng, G.; Wang, X.; Li, G.; Yang, D.; Ma, D.; Duan, L. TADF Molecules with *π*-Extended Acceptors for Simplified High-Efficiency Blue and White Organic Light-Emitting Diodes. *Chem* **2022**, *8* (6), 1705−1719.

(46) Li, X.; Baryshnikov, G.; Deng, C.; Bao, X.; Wu, B.; Zhou, Y.; Ågren, H.; Zhu, L. A Three-Dimensional Ratiometric Sensing Strategy on Unimolecular Fluorescence−Thermally Activated Delayed Fluorescence Dual Emission. *Nat. Commun.* **2019**, *10* (1), No. 731.

(47) Lee, Y. T.; Chan, C. Y.; Tanaka, M.; Mamada, M.; Balijapalli, U.; Tsuchiya, Y.; Nakanotani, H.; Hatakeyama, T.; Adachi, C. Investigating HOMO Energy Levels of Terminal Emitters for Realizing High-Brightness and Stable TADF-Assisted Fluorescence Organic Light-Emitting Diodes. *Adv. Electron. Mater.* **2021**, *7* (4), No. 2001090.

(48) Wei, X.; Chen, Y.; Duan, R.; Liu, J.; Wang, R.; Liu, Y.; Li, Z.; Yi, Y.; Yamada-Takamura, Y.; Wang, P.; Wang, Y. Triplet Decay-Induced Negative Temperature Dependence of the Transient Photoluminescence Decay of Thermally Activated Delayed Fluorescence Emitter. *J. Mater. Chem. C* **2017**, *5* (46), 12077−12084.

(49) Li, M.; Xie, W.; Cai, X.; Peng, X.; Liu, K.; Gu, Q.; Zhou, J.; Qiu, W.; Chen, Z.; Gan, Y.; Su, S. J. Molecular Engineering of Sulfur-Bridged Polycyclic Emitters Towards Tunable TADF and RTP Electroluminescence. *Angew. Chem., Int. Ed.* **2022**, *61* (35), No. e202209343.

(50) Zhan, L.; Tang, Y.; Ning, W.; Xie, G.; Zhong, C.; Gong, S.; Yang, C. Humidity Visualization through a Simple Thermally Activated Delayed Fluorescent Emitter: The Role of Hydrogen Bonding. *Chem. Eng. J.* **2023**, *454*, No. 140182.

(51) Schwendt, G.; Borisov, S. M. Achieving Simultaneous Sensing of Oxygen and Temperature with Metalloporphyrins Featuring Efficient Thermally Activated Delayed Fluorescence and Phosphorescence. *Sens. Actuators, B* **2023**, *393*, No. 134236.

(52) He, L.; Wang, Z.; Duan, L.; Yang, C.; Tang, R.; Song, X.; Pan, C. Toward Fluorine-Free Blue-Emitting Cationic Iridium Complexes: To Generate Emission from the Cyclometalating Ligands with Enhanced Triplet Energy. *Dalton Trans.* **2016**, *45* (13), 5604−5613.

(53) Kawamura, Y.; Goushi, K.; Brooks, J.; Brown, J. J.; Sasabe, H.; Adachi, C. 100% Phosphorescence Quantum Efficiency of Ir (III) Complexes in Organic Semiconductor Films. *Appl. Phys. Lett.* **2005**, *86* (7), 071104.

(54) He, L.; Lan, Y.; Ma, D.; Song, X.; Duan, L. Fluorine-Free, Highly Efficient, Blue-Green and Sky-Blue-Emitting Cationic Iridium Complexes and Their Use for Efficient Organic Light-Emitting Diodes. *J. Mater. Chem. C* **2018**, *6* (6), 1509−1520.

(55) Zhang, G.; Hermerschmidt, F.; Pramanik, A.; Schollmeyer, D.; Baumgarten, M.; Sarkar, P.; List-Kratochvil, E. J. W.; Müllen, K. Bulky, Dendronized Iridium Complexes and Their Photoluminescence. *J. Mater. Chem. C* **2019**, *7* (48), 15252−15258.

(56) Wang, X. Y.; Lv, L.; Sun, L.; Hou, Y.; Hou, Z.; Chen, Z. Recent Advances in Mechanochromism of Metal-Organic Compounds. *Front. Chem.* **2022**, *10*, No. 865198.

(57) Nasiri, S.; Dashti, A.; Hosseinnezhad, M.; Rabiei, M.; Palevicius, A.; Doustmohammadi, A.; Janusas, G. Mechanochromic and Thermally Activated Delayed Fluorescence Dyes Obtained from D−A−D′ Type, Consisted of Xanthen and Carbazole Derivatives as an Emitter Layer in Organic Light Emitting Diodes. *Chem. Eng. J.* **2022**, *430*, No. 131877.

(58) Sun, X.; Zhang, X.; Li, X.; Liu, S.; Zhang, G. A Mechanistic Investigation of Mechanochromic Luminescent Organoboron Materials. *J. Mater. Chem.* **2012**, *22* (33), 17332−17339.

(59) Weber, W. J.; Kinsler-Fedon, C.; Keppens, V.; Zhang, Y.; Mir, A. H. Temperature Dependence of Irradiation-Induced Amorphization in a High-Entropy Titanate Pyrochlore. *MRS Commun.* **2024**, *14* (6), 1364−1370.

(60) Ryder, M. R.; Bennett, T. D.; Kelley, C. S.; Frogley, M. D.; Cinque, G.; Tan, J. C. Tracking Thermal-Induced Amorphization of a Zeolitic Imidazolate Framework via Synchrotron in Situ Far-Infrared Spectroscopy. *Chem. Commun.* **2017**, *53* (52), 7041−7044.

(61) Nafees, A.; Kalita, G.; Paul, M. K.; Sinha, A.; Rao, N. V. S. Effect of Methoxy Group Instead of Polar Group in the Nematic Phase of Four-Ring Bent-Core Liquid Crystals. *RSC Adv.* **2015**, *5* (9), 7001−7006.

(62) Selvakumar, N.; Khera, M. K.; Reddy, B. Y.; Srinivas, D.; Azhagan, A. M.; Iqbal, J. An Efficient Total Synthesis of 9-Methoxycarbazole-3-Carbaldehyde Based on a Novel Methodology for the Preparation of Methoxyindoles. *Tetrahedron Lett.* **2003**, *44* (37), 7071−7074.

(63) D'andrade, B. W.; Forrest, S. R.; Wang, F.; Tao, X. M.; Wang, R. X. Multilayer Transparent Electrode for Organic Light-Emitting Diodes: Tuning Its Optical Characteristics. *Opt. Express* **2010**, *18* (4), 3404−3414.

(64) Wang, C.; Wang, C.; Huang, Z.; Xu, S. Materials and Structures toward Soft Electronics. *Adv. Mater.* **2018**, *30* (50), No. 1801368.

(65) Palanisamy, P.; Rabiei, M.; Hosseinnezhad, M.; Palevicius, A.; Janusas, G.; Managutti, P. B.; Mohamed, S.; de Sousa, L. E.; de Thieulloy, L.; de Silva, P.; Vilkauskas, A.; Nasiri, S.; Nunzi, J. M.; Nutalapati, V. Solution-Processed OLEDs Based on a Bipolar AIE Terpyridine Derivative as a Host. *ACS Appl. Opt. Mater.* **2024**, *2* (1), 76−87.

(66) Pang, X.; Zhang, K.; Song, Y.; Xiu, Y.; Yu, R.; He, L. Intrinsically-Ionic Donor-Acceptor Molecules Featuring Thermally-Activated Delayed Fluorescence for High-Performance Host-Guest Blue Light-Emitting Electrochemical Cells. *Chem. Eng. J.* **2022**, *450*, No. 137987.

(67) Anandan, M.; Kment, S.; Zboril, R.; Kalytchuk, S.; Janusas, G.; Managutti, P. B.; Mohamed, S.; Mazloumihaghghi, R.; Hosseinnezhad, M.; Nunzi, J. M.; Nutalapati, V.; Nasiri, S. High Triplet Hexahydroacridine Derivatives as a Host Prevent Exciton Diffusion to Adjacent Layers in Solution Processed OLEDs. *Org. Electron.* **2025**, *136*, No. 107162.

(68) Rota Martir, D.; Bansal, A. K.; Di Mascio, V.; Cordes, D. B.; Henwood, A. F.; Slawin, A. M. Z.; Kamer, P. C. J.; Martínez-Sarti, L.; Pertegás, A.; Bolink, H. J.; Samuel, I. D. W.; Zysman-Colman, E. Enhancing the Photoluminescence Quantum Yields of Blue-Emitting Cationic Iridium(III) Complexes Bearing Bisphosphine Ligands. *Inorg. Chem. Front.* **2016**, *3* (2), 218−235.

(69) Shin, J. H.; Matyba, P.; Robinson, N. D.; Edman, L. The Influence of Electrodes on the Performance of Light-Emitting Electrochemical Cells. *Electrochim. Acta* **2007**, *52* (23), 6456−6462.